Nanoscale

PAPER

Check for updates

Engineering 3D structure Mn/YTiO$_x$ nanotube catalyst with an efficient H$_2$O and SO$_2$ tolerance for low-temperature selective catalytic reduction of NO with NH$_3$†

Rongji Cui,[a,b] Xiaosheng Huang, [ID] [a] Guodong Zhang[a] and Zhicheng Tang [ID] ★[a,b]

TiO$_2$ with a 3D structure is considered to be a promising support for Mn-based catalysts for the NH$_3$-SCR reaction, but it is still insufficient to solve problems such as poor N$_2$ selectivity and tolerance of H$_2$O/SO$_2$ at low temperature. In this work, a novel 3D-structured Mn/YTiO$_x$ nanotube catalyst was designed and the role of Y on the catalytic performance was investigated for the NH$_3$-SCR reaction at low temperature. The results indicated that the Y-doped TiO$_x$ gradually transformed from nanotubes to nanosheets with the increase in Y doping, leading to a reduction in specific surface area and Brønsted acid sites. An appropriate amount of Y doping could distinctly improve the dispersion of MnO$_x$ and increase the concentration of surface Mn^{4+}, Lewis acid sites and chemisorbed oxygen of catalysts, which was beneficial to the low-temperature NH$_3$-SCR reaction, while excessive Y doping could cause a sharp decrease in specific surface area and Lewis acid sites. Therefore, Mn/YTiO$_x$ catalysts exhibited a volcano-type tendency in NO conversion with an increase in Y doping, and the highest activity was obtained at 3% doping, showing more than 90% NO conversion and N$_2$ selectivity in a wide temperature window from 120 to 320 °C. The N$_2$ selectivity and H$_2$O/SO$_2$ resistance of the catalysts was also enhanced with the increase in Y doping mainly due to the increased chemisorbed oxygen and electron transfer between Y and Mn. An in situ DRIFTS study demonstrated that Lewis acid sites played a more important role in the reaction than Brønsted acid sites, and the coordinated NH$_3$ absorbed on Lewis acid sites, −NH$_2$, monodentate nitrate and free nitrate ions were the main reactive intermediate species in the NH$_3$-SCR reaction over an Mn/3% YTiO$_x$ catalyst. Langmuir−Hinshelwood (L−H) and Eley−Rideal (E−R) reaction mechanisms co-existed in the NH$_3$-SCR reaction, but the L−H reaction mechanism predominated.

1. Introduction

Nitrogen oxides (NO$_x$) emitted from the combustion of mobile and stationary sources has triggered a series of severe environmental issues, including photochemical smog, acid rain and ozone layer depletion, which cause serious damage to the ecological environment and human health.[1] As the state-of-the-art denitrification strategy, the selective catalytic reduction of NO$_x$ with NH$_3$ (NH$_3$-SCR) has realized extensive applications in the removal of stationary source NO$_x$. However, in cement, glass, steel and other non-electric industries, the NH$_3$-SCR units are placed downstream of the electrostatic precipitator and the desulfurization units to avoid poisoning of the catalyst by SO$_2$ and dust, to prolong its lifetime as long as possible. This leads to a reduction in the flue gas temperature, even below 200 °C, and reheating of the exhaust gas to reach the operating temperature of vanadium-based catalysts undoubtedly increases the operating cost and reduces the economy of the process. Therefore, considerable effort has been devoted to the development of vanadium-free catalysts for NH$_3$-SCR at low temperature. Manganese-based catalysts exhibit remarkable catalytic performance in low-temperature NH$_3$-SCR due to their multiple oxidation states and labile oxygen, which can promote the adsorption and activation of reactants on the surface. However, N$_2$ selectivity and H$_2$O/SO$_2$ tolerance of manganese-based catalysts at low temperature still need to be further improved before achieving industrial commercialization.

[a]State Key Laboratory for Oxo Synthesis and Selective Oxidation, National Engineering Research Center for Fine Petrochemical Intermediates, Lanzhou Institute of Chemical Physics, Chinese Academy of Sciences, Lanzhou 730000, China.
E-mail: tangzhicheng@licp.cas.cn
[b]Shandong Laboratory of Yantai Advanced Materials and Green Manufacturing, Yantai Zhongke Research Institute of Advanced Materials and Green Chemical Engineering, Yantai, 264006, China
†Electronic supplementary information (ESI) available. See DOI: https://doi.org/10.1039/d2nr07304h

Rare earth metal doping is a common method to enhance the catalytic ability of Mn-based catalysts due to the unique 4f electron orbit ensuring superior performance of oxygen storage and release.[2] It is reported that Ce doping can not only provide rich active oxygen to accelerate the redox circle of $Mn^{3+} + Ce^{4+} \leftrightarrow Mn^{4+} + Ce^{3+}$, thus improving catalytic efficiency, but also promoting the formation of bulk-like sulfate and alleviating the poisoning of SO_2 to MnO_x by preferentially reacting with SO_2.[3] The effect of Sm doping on an Mn-based catalyst was studied by Meng et al.,[4] and the results showed the promotion effect of Y doping on the increase in the amount of surface active oxygen and Mn^{4+} and specific surface area, thus improving the absorption and activation ability for NH_3 and NO. Moreover, an enhancement in resistance to both H_2O and SO_2 was obviously observed. Similarly, doping of Eu could also increase the concentration of chemisorbed oxygen and surface Mn^{4+}, restraining the crystallization of MnO_x, hinder the generation of ammonium sulfate and maintain better adsorption capacity for NH_3.[5,6] Yu found that doping Pr into MnO_x/SAPO-34 catalysts could prevent active components from sulfation and inhibit the generation of ammonia bisulfate.[7] Niu et al.[8] indicated that doping with Tm could improve the surface acidity and reducibility of Mn-based catalysts, contributing to the adsorption and activation of NH_3 and NO. Zhang et al.[9] developed Y-doped TiO_2 by replacing Ti^{4+} with Y^{3+}, followed by MnO_x loading. It was found that the catalytic efficiency was improved due to the increasing amount of superoxide ions in surface active oxygen and NO oxidation, which was generated from the interaction between WO_3 and TiO_2 owing to F doping. Thus, the role of rare earth metals in the NH_3-SCR reaction is mainly reflected in an improvement in the redox ability and SO_2/H_2O tolerance of Mn-based catalysts.

TiO_2 has been widely used as a carrier of catalysts in the NH_3-SCR reaction owing to the advantages of chemical stability, non-toxicity and easy access, and the morphologies of TiO_2 are reported to have a significant effect on catalytic ability. In our previous work,[10] flower-like TiO_2 as a support contributed to improving catalytic activity and resistance to H_2O and SO_2 by increasing the surface atomic ratio of Ce^{3+}/$(Ce^{3+} + Ce^{4+})$, surface active oxygen and the acid property. Besides, Qin et al.[11] pointed out that the unique flower-like structure can improve the dispersion and interaction of the active species Mn and Ce, thereby facilitating the "fast SCR" reaction. Cheng et al.[12] suggested that 3D TiO_2 microspheres consisting of nanorods can promote the dispersion of CeO_2 through a strong interaction with CeO_2, and enhance the surface acidity, oxygen vacancies and redox property of the catalyst, hence improving the catalytic ability. TiO_2 nanosheets exposed with (001) facets (TiO_2-NS) were prepared by Li et al.,[13] and it was proved to improve the specific surface area and the amount of chemisorbed oxygen and acid sites. The catalytic efficiency of the Mn–Ce/TiO_2-NP catalyst was 30% lower than that of Mn–Ce/TiO_2-NS in the temperature range 100–160 °C. Furthermore, TiO_2 nanotubes are at the leading edge of TiO_2 nano-materials, and are recognized as promising supports for

SCR catalysts. The special nano-tubular structure and large surface area of TiO_2 nanotubes are conducive to the high dispersion of active species and short diffusion length of reaction gases, which greatly increase the NO_x conversion of catalysts at 100–300 °C.[14] Likewise, Cu supported on TiO_2 nanotubes has been reported to exhibit much higher NO conversion as well as excellent N_2 selectivity compared with that supported on TiO_2 nanoparticles, owing to a strong redox property and adsorption capability.[15] Furthermore, the confinement effect of nanotubes can not only effectively reduce the grain size of active components, but also prevent them from sulfation.[16,17]

As mentioned above, both regulating the morphology of the TiO_2 support and doping with rare earth metals can improve the catalytic performance and H_2O/SO_2 tolerance of Mn-based catalysts. Enlightened by these facts, we added rare earth metal Y to the mixture of TiO_2 powder and NaOH for the hydrothermal synthesis of titanium nanotubes in this work. The impact of Y doping on the physicochemical properties of TiO_2 nanotubes, and the further effect on catalytic performance of Y-doped TiO_2 supported MnO_x catalysts was investigated through a variety of characterization methods and tests of the catalytic ability and tolerance of H_2O/SO_2. In situ DRIFTS experiments were also carried out to explore the mechanism of the NH_3-SCR reaction over the Y-doped TiO_x supported MnO_x catalyst.

2. Experimental section

2.1. Synthesis of TiO_2-NT and $YTiO_x$

The TiO_2 nanotubes were synthesized by a typical hydrothermal treatment reported in the literature.[18] First, 2.5 g of commercial P25 TiO_2 powder (Degussa, Germany) was dissolved in 70 mL of 10 M NaOH solution in a Teflon-lined autoclave, and hydrothermally treated at 150 °C for 24 h. After the hydrothermal treatment, the slurry was filtered, washed with deionized water several times until the pH was close to 7, and then dispersed in 0.1 M HCl solution. After stirring for two hours, the mixture was washed again with deionized water until neutral, then dried at 80 °C for 12 h, ground in a mortar and calcined at 400 °C for 2.5 h. Finally, the resulting TiO_2 nanotubes were prepared, and denoted TiO_2-NT. The preparation process for Y-doped TiO_2 with a doping amount of 1%–5% followed the aforementioned method, except that $Y(NO_3)_3 \cdot 6H_2O$ was initially added to the mixture of TiO_2 powder and NaOH, and the doping amount refers to the molar ratio of Y to Ti. The resulting Y-doped TiO_2 were denoted 1%$YTiO_x$, 3%$YTiO_x$ and 5%$YTiO_x$, respectively.

2.2. Synthesis of Mn/TiO_2-NT and Mn/$YTiO_x$

Y-doped TiO_2 nanotubes with 15% manganese loading were carried out by a vacuum-assisted incipient-wetness impregnation method. An $Mn(NO_3)_2$ solution of required concentration was dropped onto the support, and the resulting mixture was left for 12 h in a vacuum environment, followed by 12 hours of drying at 80 °C and 4 hours of calcining at

450 °C. The resulting catalysts were obtained and denoted Mn/TiO$_2$-NT, Mn/1%YTiO$_x$, Mn/3%YTiO$_x$ and Mn/5%YTiO$_x$, respectively, according to the doping ratio of Y on the support.

2.3. Catalyst characterization

The instruments and methods used for characterization are detailed in the ESI.†

2.4. Catalytic performance evaluation

The experimental description and calculation method of catalyst performance evaluation are described in ESI.†

3. Results and discussion

3.1. Bulk structure analysis

Fig. 1 shows the XRD patterns of Y-doped TiO$_2$ and its supported MnO$_x$ catalysts. It can be observed from Fig. 1(a) that

Fig. 1 XRD patterns of (a) Y-doped TiO$_2$, (b) Y-doped TiO$_2$ supported MnO$_x$ catalysts.

TiO$_2$ nanotubes without Y doping exhibited peaks at 2θ = 25.3, 37.7, 48.0, 53.8, and 55.0°, which are ascribed to the standard XRD patterns of anatase (JCPDS, card 21-1272).[19] This revealed that anatase TiO$_2$ was the main crystal phase of the tube wall of TiO$_2$ nanotubes synthesized by the traditional alkaline hydrothermal method. When doping with 1% Y, the full width at half maximum intensity of the (101) diffraction line of the anatase phase (FWHM, 2θ = 25.3°) increased from 1.03 to 1.12, suggesting a decrease in crystallinity. This was mainly due to the partial substitution of Ti^{4+} in the TiO$_2$ lattice by Y^{3+} during hydrothermal synthesis and the lattice distortion caused by the different ionic radii of Y^{3+} (0.089 nm) and Ti^{4+} (0.068 nm). When the doping amount increased to 3% and 5%, the characteristic peaks of anatase disappeared completely accompanied by the emergence of two diffuse peaks at 2θ = 26.5 and 48.7°, which were ascribed to layered protonated titanate (JCPDS, card 47-0124) with poor crystallinity.[20] In addition, no characteristic peaks related to Y$_2$O$_3$ can be observed in the XRD patterns of all supports owing to the low content and high dispersion of Y$_2$O$_3$ in titanate. After loading manganese, three peaks at 28.8, 57.4 and 37.7° can be observed on the Mn/TiO$_2$-NT catalyst (Fig. 1b) in addition to the characteristic peaks of anatase, which were assigned to the typical XRD patterns of manganese oxide (JCPDS, card 24-0735).[21] But it is worth noting that the peak intensity of manganese oxide decreased at 1% Y doping and disappeared at 3% and 5% Y doping, indicating that Y doping in TiO$_2$ greatly improved the dispersion of manganese oxide on the TiO$_x$ support. Interestingly, the characteristic peaks of anatase rather than protonated titanate were observed in Mn/3%YTiO$_x$ and Mn/5%YTiO$_x$, which may be due to the protonated titanate in the supports being transformed into anatase TiO$_2$ again after manganese loading and calcination treatment.

The crystalline phase structure of the supports and catalysts were studied by Raman spectroscopy. As shown in Fig. 2(a), TiO$_2$-NT presented five Raman bands at 144, 197, 397, 515 and 638 cm^{-1}, corresponding to the Raman vibration modes of E$_g$, E$_g$, B$_{1g}$, A$_{1g}$ + B$_{1g}$ and E$_g$, respectively. The six Raman modes (A$_{1g}$ + 2B$_{1g}$ + 3E$_g$) perfectly match the crystal structure of anatase TiO$_2$.[22] With the addition of 1% Y, the FWHM of the Raman peak at 144 cm^{-1} increased, implying the variation of Ti–O–Ti bands in octahedral TiO$_6$. When doping with 3% Y, the Raman bands related to anatase TiO$_2$ disappeared, and bands at 148, 281, 450 and 701 cm^{-1} were observed, which were assigned to the Ti–O–Ti vibrations for layered lepidocrocite titanate (H$_x$Ti$_{2-x/4}\square_{x/4}$O$_4$, where $\square$ represents a vacancy), a kind of protonated titanate.[23] This indicated that the main component of the support had changed from anatase TiO$_2$ to layered lepidocrocite titanate at 3% Y doping, which was consistent with the XRD results. As the doping amount increased to 5%, the Raman peaks were further enhanced in intensity. Only Raman peaks of anatase TiO$_2$ can be observed in the Mn/TiO$_2$-NT and Mn/1%YTiO$_x$ catalysts in Fig. 2(b). The Mn/3%YTiO$_x$ and Mn/5%YTiO$_x$ catalysts showed the Raman peaks of layered lepidocrocite titanate whose intensities were significantly lower than those of their respective supports, as well as
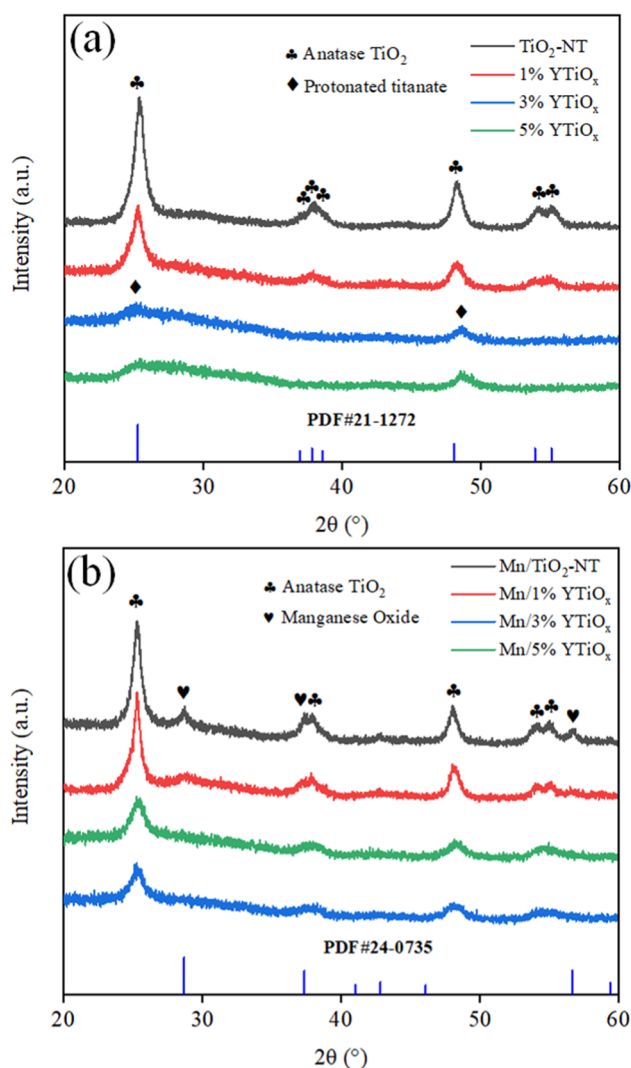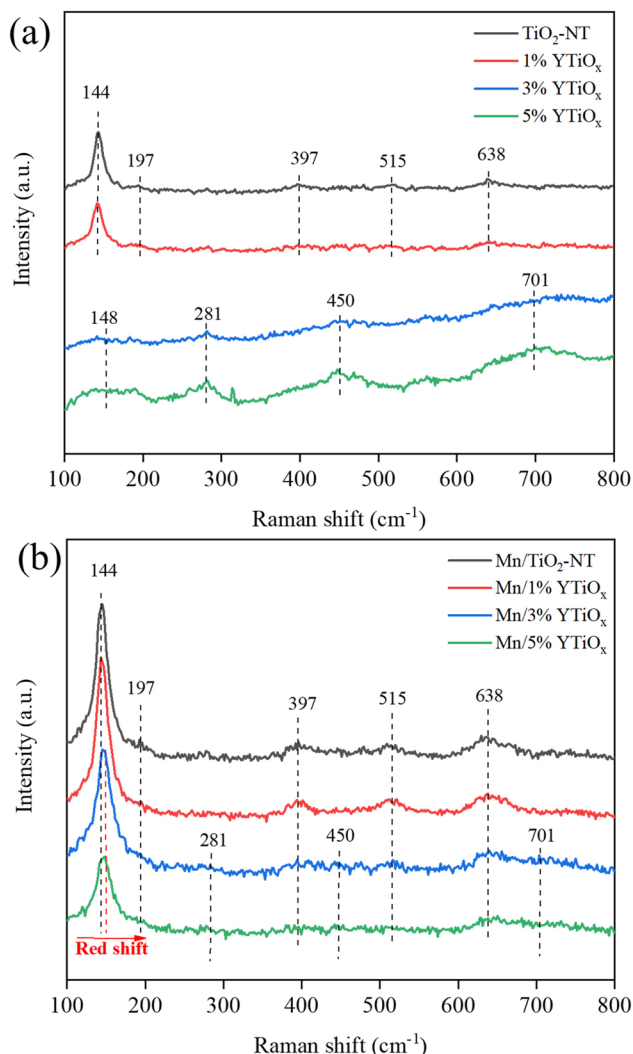
Fig. 2 Raman spectra of Y-doped TiO$_2$ supported MnO$_x$ catalysts.

Fig. 3 (a) N$_2$ adsorption–desorption isotherms, (b) pore size distributions of Y-doped TiO$_2$.

anatase TiO$_2$ which was not observed in their supports. This phenomenon proved again that Mn loading could lead to transformation from layered lepidocrocite titanate to anatase TiO$_2$. It can be speculated that Mn ions were inserted into the cationic vacancies of layered lepidocrocite titanate during the process of loading, thus inducing structural re-arrangement to reach a stable state, which also explained why Y doping could improve the dispersion of MnO$_x$. A red shift and weakening of anatase TiO$_2$ bands can be seen from Mn/1% YTiO$_x$ to Mn/5%YTiO$_x$, which were ascribed to the enhanced lattice distortion and increased oxygen vacancies caused by Y doping. In addition, no Raman bands for MnO$_x$ or Y$_2$O$_3$ were detected in the catalysts due to the good dispersion on the supports.

Fig. 3 displays N$_2$ adsorption–desorption isotherms and pore size distributions of Y-doped TiO$_2$. The textual parameters of Y-doped TiO$_2$ are summarized in Table 1. TiO$_2$-NT and 1%YTiO$_x$ showed typical IV curves with hysteresis loops of type H3 assigned to the characterization of crack-like pores
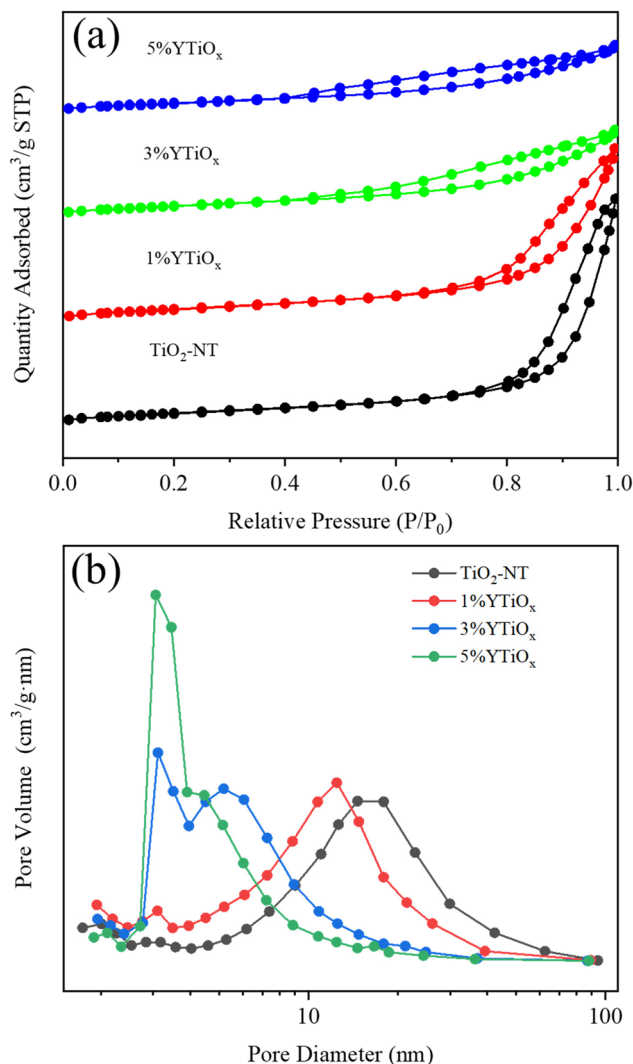
Table 1 Summary of specific surface area, pore volume and average pore diameter

Sample	Specific surface area (m^2 g^{-1})	Pore volume (cm^3 g^{-1})	Average pore diameter (nm)
TiO$_2$-NT	250.50	1.38	17.87
1%YTiO$_x$	246.01	1.05	13.21
3%YTiO$_x$	218.06	0.55	7.10
5%YTiO$_x$	191.94	0.43	5.79

resulting from the curling-up of nanosheets.[24] Moreover, the unique hollow tubular structure of TiO$_2$-NT led to a high specific surface area of 250.50 m^2 g^{-1} and pore volume of 1.38 cm^3 g^{-1}. For 3%YTiO$_x$ and 5%YTiO$_x$, the isotherms similarly exhibited a typical IV curve, but with the loop at a relative pressure above 0.4, suggesting the existence of mesopores from stacked nanosheets.[25] The change in pore structure was directly reflected in the specific surface and pore volume, and

pore diameter. When the doping amount increased from 1% to 5%, the specific surface area decreased from 246.01 to 191.94 m^2 g^{-1}, the pore volume decreased from 1.05 to 0.43 cm^3 g^{-1} and the averaged pore diameter decreased from 13.21 to 5.79 nm. It can be concluded that the morphology of the support changed from nanotubes to nanosheets with the increase in Y doping, resulting in a reduction in specific surface area, pore volume and mean pore diameter. In particular, when the doping amount reached 5%, the specific surface area of the support was significantly reduced, which was unfavorable for the adsorption and diffusion of reactants.

3.2. TEM analysis

The morphological characterization and microstructure of the supports and catalysts were further investigated through high resolution transmission electron microscopy (TEM/HR-TEM). The TEM and HR-TEM images of TiO_2-NT, 1%$YTiO_x$, 3%$YTiO_x$, 5%$YTiO_x$ and Mn/3%$YTiO_x$ are depicted in Fig. 4. It can be observed that TiO_2-NT displayed an open-ended nanotubular structure of 100–200 nm in length. The uniform outer and inner diameter for TiO_2-NT were 12 nm and 6 nm, respectively (Fig. 4a). This indicated that the TiO_2 nanotubes can be

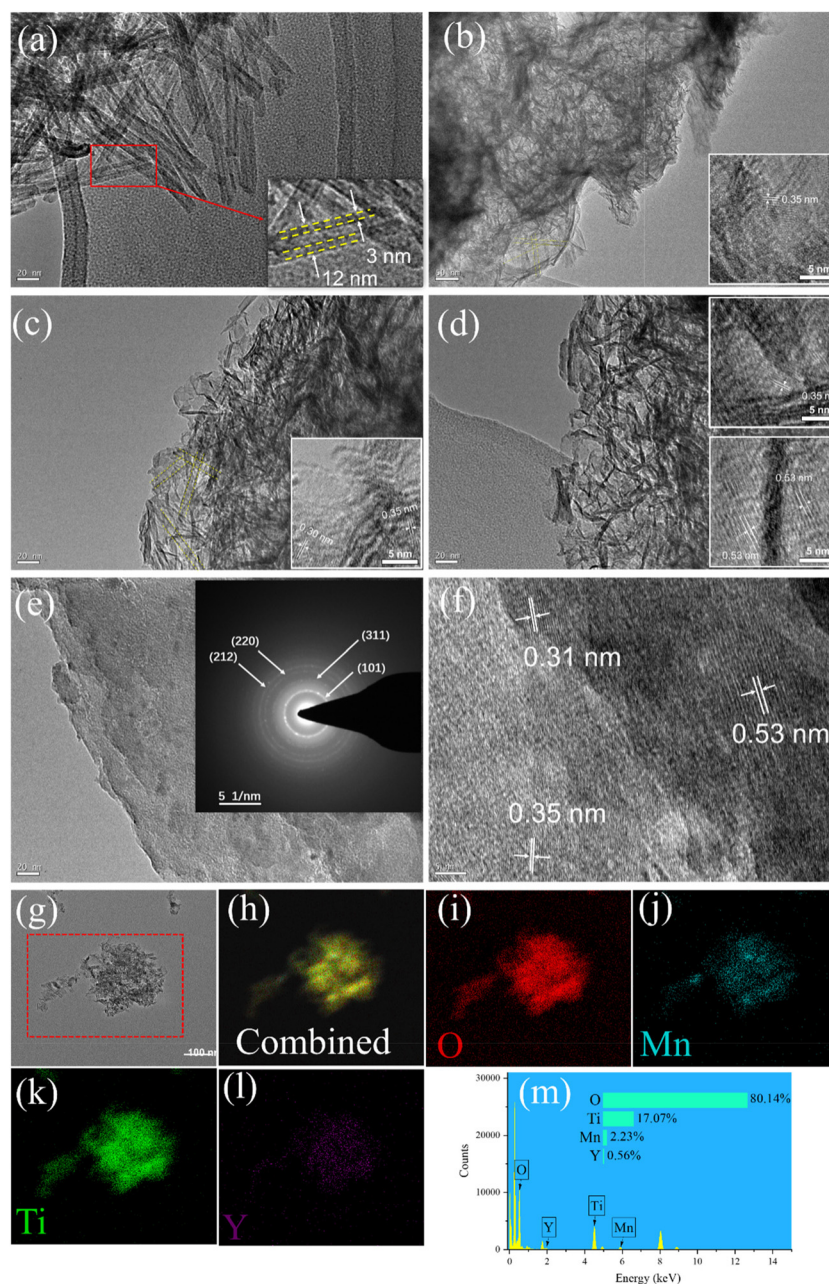**Fig. 4** TEM and HR-TEM images of (a) TiO_2-NT, (b) 1%$YTiO_x$, (c) 3%$YTiO_x$, (d) 5%$YTiO_x$ and (e–f) Mn/3%$YTiO_x$ and (g–m) EDX-mapping of Mn/3%$YTiO_x$.

prepared successfully from a TiO$_2$ precursor (Degussa P25) under current experimental conditions. Whereas well-defined nanotubes were significantly changed due to the addition of Y species, as shown in Fig. 4(b). While some nanotube structure can still be observed, a large number of nanosheets and nano-rolls are present in the TEM image. The *d*-spacing of the lattice fringes in 1%YTiO$_x$ was measured as 0.35 nm, which is close to the (101) plane of TiO$_2$.[26] It is generally recognized that tita-nate nanosheets are first formed from TiO$_2$ nanoparticles in a concentrated solution of NaOH, and then are slowly rolled into semi-finished nanotubes of short size under high temperature and high pressure, which are finally grown into finished nano-tubes with a complete structure through the dissolution–repre-cipitation mechanism.[27] The presence of a large number of nanosheets and nanorolls, as shown in Fig. 4(b), revealed that the process of rolling nanosheets into nanotubes was greatly restricted due to the destruction of the anatase crystal phase by Y doping.

As displayed in Fig. 4(c), when doped with 3% Y species, a small amount of nanotubes can still be observed, and the rest were mainly nanosheets. The crystal plane (101) of TiO$_2$ and the crystal plane (222) of Y$_2$O$_3$ were observed, corresponding to the lattice fringes measured at 0.35 and 0.30 nm, respectively. This illustrated that Y species were well doped in the titanium nanosheets by partially substituting Ti^{4+} in the hydrothermal process. When doped with 5% Y, the nanotubes can hardly be observed in the obtained products, as shown in Fig. 4(d). From the HRTEM images, 5%YTiO$_x$ displayed distinct lattice fringes with an interlayer spacing of 0.35 and 0.53 nm, and the latter could be classified as the (200) plane of Y$_2$O$_3$. As shown in Fig. 4(e), MnO$_x$ loading makes the original nanosheets fuse together without obvious agglomeration in the Mn/3%YTiO$_x$ catalyst, indicating that the MnO$_x$ components had good dis-persion on 3%YTiO$_x$. Moreover, the distinct diffraction rings were well attributed to the (101) and (212) planes of MnO$_2$ (400), and the (220) and (311) planes of Mn$_3$O$_4$. As depicted in Fig. 4(f), lattice fringes with a distance of 0.31 nm ascribed to the (110) plane of MnO$_2$ and lattice fringes corresponding to the (200) plane of Y$_2$O$_3$ and the (101) plane of TiO$_2$ were detected. As shown in Fig. 4(g–l), a high dispersion of Mn, Y, Ti and O was observed, indicating the uniform doping of Y in TiO$_2$ and the even loading of Mn on the support.

3.3. H$_2$-TPR analysis

The H$_2$-TPR results of Y-doped TiO$_2$ and Y-doped TiO$_2$ sup-ported MnO$_x$ catalysts are depicted in Fig. S1† and Fig. 5. As shown in Fig. S1,† a weak peak at 573 °C for TiO$_2$-NT was related to the reduction of Ti^{4+} to Ti^{3+}, and the small peak area indicated that the reduction of TiO$_2$ is difficult.[28] However, the reduction peak at 570 °C for the Mn/1%YTiOx catalyst was mainly assigned to the reduction of Y$_2$O$_3$.[29] It was clearly seen that the peak intensity and temperature of Y$_2$O$_3$ reduction increased with the increasing amount of Y doping, which may be due to the increase in Y content in TiO$_2$ and the enhance-ment of the interaction between Y and TiO$_2$, respectively. It can be observed from Fig. 5 that Mn/TiO$_2$-NT showed two
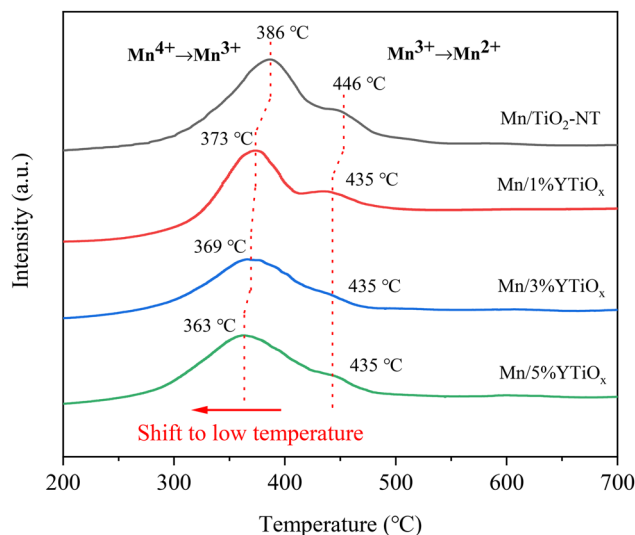

Fig. 5 H$_2$-TPR profiles of Mn/TiO$_2$-NT and Y-doped TiO$_2$ supported MnO$_x$ catalysts.

reduction peaks at 386 °C and 446 °C, which could be attribu-ted to the reduction of Mn^{4+} to Mn^{3+} and Mn^{3+} to Mn^{2+}, respectively.[14,30] However, the reduction peaks of Mn^{4+} to Mn^{3+} and Mn^{3+} to Mn^{2+} shifted toward low temperature with an increase in Y doping amount, suggesting that Y doping could effectively improve the reducibility of Mn-based cata-lysts. In conjunction with the above discussion, the enhance-ment of reducibility may be related to the smaller MnOx grain size due to the high dispersion and the increased surface oxygen mobility caused by the abundant oxygen vacancies. Besides, as a rare earth element, the excellent oxygen storage and release performance of Y and the redox cycle between Y and Mn can also accelerate the surface oxygen mobility, thereby improving the redox performance of the catalyst. However, the outstanding redox performance is generally con-sidered to greatly enhance the catalytic ability of Mn-based cat-alysts in the NH$_3$-SCR reaction.

3.4. NH$_3$-TPD analysis

Considering the important role of catalyst acidity in NH$_3$ adsorption and activation, the amount and strength of surface acid sites of Y-doped TiO$_2$ and Y-doped TiO$_2$ supported MnO$_x$ catalysts were investigated and the NH$_3$-TPD profiles are pre-sented in Fig. S2† and Fig. 6, respectively. As presented in Fig. S2,† TiO$_2$-NT showed two NH$_3$ desorption peaks at about 200 °C and 350 °C, corresponding to desorption of NH$_3$ adsorbed on weak acid sites and medium strong acid sites of the catalysts, respectively. For TiO$_2$ nanotubes, the weak acid sites are derived from Lewis acid sites brought about by the coordination of the unsaturated Ti^{4+} structure and the medium strong acid sites originate from Brønsted acid sites stemming from the Ti–OH groups.[31] It is obvious from 1% YTiO$_x$ that Y doping can distinctly diminish the medium strong acid sites of TiO$_2$-NT. Masaaki *et al.*[32] reported that
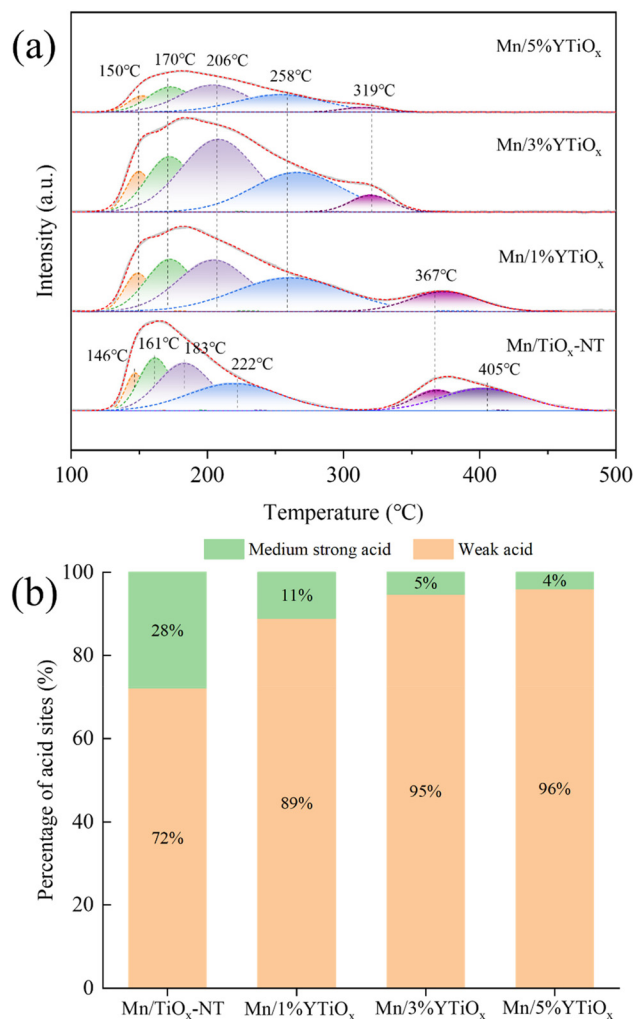
Fig. 6 NH$_3$-TPD profiles (a) and percentages of surface acidity (b) of Mn/TiO$_2$-NT and Y-doped TiO$_2$ supported MnO$_x$ catalysts.

Brønsted acid sites could be effectively formed from the lattice distortion caused by the scrolling of titanate nanosheets. Therefore, the sharp decrease in the amount of Brønsted acid sites may be related to the morphological transformation from nanotubes to nanosheets due to Y doping. Moreover, the amount of weak acid sites was gradually reduced with the increase in Y doping amount. This can be ascribed to the increase in the amount of layered lepidocrocite titanate and the decrease in the specific surface area, and the amount of exposed Lewis acid sites on layered lepidocrocite titanate is much lower than that of anatase TiO$_2$.[32] As shown in Fig. 6(a), Mn loading reduced the amount and strength of weak acid sites by comparing TiO$_2$-NT and Mn/TiO$_x$-NT. Mn/TiO$_x$-NT also showed a lower amount of medium strong acid than TiO$_2$-NT, which was attributed to the replacement of H$^+$ in Brønsted acid sites by Mn^{4+} during the impregnation process. For Y-doped TiO$_2$ supported MnO$_x$ catalysts, they all exhibit four peaks at temperatures below 300 °C and one peak at temperatures above 300 °C, related to weak acid and medium strong

acid, respectively. The strength and amount of medium strong acid decreased with an increase in Y doping, while the amount of weak acid increased first and then decreased with an increase in Y doping amount. Combined with Raman, BET and TPR results, it was believed that the increase in the amount of oxygen vacancies caused by Y doping could lead to an increase in the amount of unsaturated Ti^{4+} and high-valence Mn ions, which acted as Lewis acid sites, and finally showed an increase in weak acid sites from Mn/TiO$_2$-NT to Mn/3%YTiO$_x$ catalysts. However, the sharp decrease in weak acid sites of the Mn/5%YTiO$_x$ catalyst may be related to the obvious reduction in its specific surface area and pore volume. In addition, it can obviously be observed from Fig. 6(b) that the ratio between weak acid and medium strong acid increased with an increase in doping amount.

3.5. XPS analysis

XPS was performed to analyze the surface chemical compositions and chemical states of the elements present in the catalysts. Mn 2p, O 1s, Y 3d and Ti 2p spectra of the catalysts are demonstrated in Fig. 7 and Fig. S3,† and were deconvoluted by the Gaussian–Lorentzian curve fitting method for identification of the chemical states of these elements, and the relative amount of different elements and their different valence states are summarized in Table 2 and Table S1.† The measured ratios of Y/Ti of the catalysts were consistent with the calculated values, while the measured ratios of Mn/Ti of the catalysts were slightly lower than the calculated values, as shown in Table S1.† In Fig. 7(a), two peaks at 638–648 eV and 648–658 eV can clearly be observed in the Mn 2p spectra for all catalysts, which were ascribed to the spin–orbital peaks of Mn 2p$_{3/2}$ and Mn 2p$_{1/2}$. Through peak-fitting deconvolution, the Mn 2p$_{3/2}$ peaks were divided into four peaks centered on 640.7, 641.6, 643.0 and 646.7 eV, corresponding to Mn^{2+}, Mn^{3+}, Mn^{4+} and the satellite peak.[33] As can be observed from Table 2, the ratio of Mn^{4+}/Mn for Mn/TiO$_2$-NT was 29.8%, but the ratio for Mn/1%YTiO$_x$ was 45.5%, and the value went up slightly and then decreased with increasing Y doping amount, reaching a maximum at 3% doping content. This indicated that the content of Mn^{4+} can be increased due to the presence of more oxygen vacancies caused by doping with an appropriate amount of Y, while the Mn^{4+} species and the redox cycle between Mn^{4+} and Mn^{3+} were considered to play a crucial role in the low-temperature NH$_3$-SCR reaction by promoting NO oxidation to NO$_2$.[34] However, the ratio of Mn^{4+}/Mn^{3+} was decreased as the Y doping amount increased from 1% to 5%, which showed that the decreased Mn^{4+} content of the Mn/5%YTiOx catalyst may be attributed to the enhanced reduction of Mn^{4+} to Mn^{3+}.

As exhibited in Fig. 7(b), two peaks centered at about 157.6 eV and 159.7 eV were detected in the Y 3d spectra of all the catalysts and are related to the spin–orbital peaks of Y 3d$_{5/2}$ and Y 3d$_{3/2}$, respectively. The Y 3d$_{5/2}$ peaks were divided into two peaks centered on 156.9 and 157.7 eV, corresponding to Y^{2+} and Y^{3+}, respectively.[35] It can clearly be observed that the content of Y^{3+} and the ratio of Y^{3+}/Y^{2+} were improved with increasing amount of Y doping. The opposite change in ratios
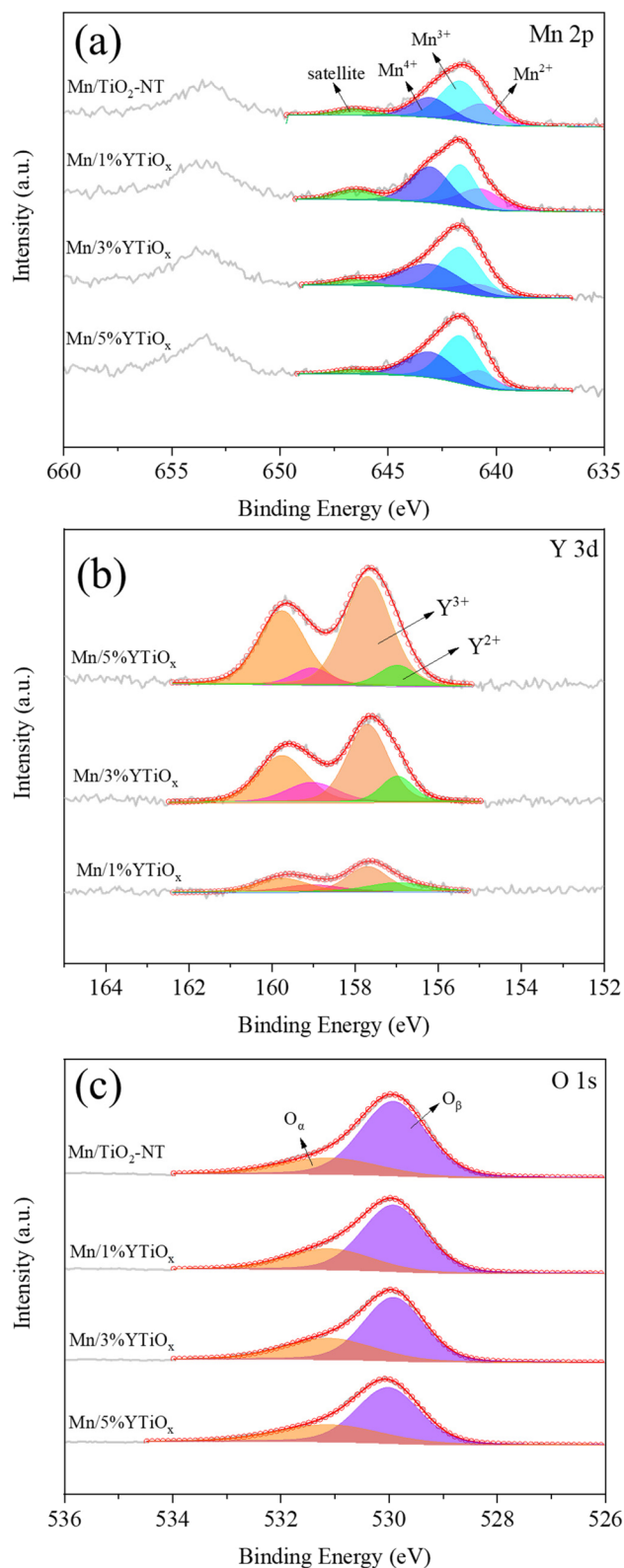
Fig. 7 Mn 2p (a), Y 3d (b) and O 1s (c) XPS spectra of Y-doped TiO$_2$ supported MnO$_x$ catalysts.

of Mn^{4+}/Mn^{3+} and Y^{3+}/Y^{2+} with increasing Y indicated that there was electron transfer from Y to Mn in the catalysts through the redox cycle of Mn^{4+} + Y^{2+} ↔ Mn^{3+} + Y^{3+}, and this redox cycle was also reflected in the H$_2$-TPR results.

As shown in Fig. 7(c), the peaks located at 531.1 eV can be assigned to the surface oxygen species (O$_\alpha$) including hydroxyl-like groups and surface chemisorbed oxygen, and the other peaks located at 529.9 eV were ascribed to the lattice oxygen species (O$_\beta$).[30] Compared with O$_\beta$, O$_\alpha$ is generally considered to be more active and has higher mobility, which plays a key role in the oxidation reaction involved.[36] The ratios of O$_\alpha$/O of Mn/1%YTiO$_x$, Mn/3%YTiO$_x$ and Mn/5%YTiO$_x$ were 30.1%, 33.8% and 33.9%, respectively, obviously higher than that of Mn/TiO$_2$-NT (25.2%), although TiO$_2$ nanotubes were claimed to be rich in surface oxygen.[37] The ratios of O$_\alpha$/O$_\beta$ increased with Y doping, suggesting that Y doping could increase the surface oxygen species by an imbalance of the charge on the catalyst surface, unsaturation of chemical bonds and the generation of vacancies.[38] It is noteworthy that the O$_\beta$ peak of Mn/5%YTiO$_x$ shifted toward higher binding energy compared with other catalysts. As displayed in Fig. S3,† the Ti 2p spectra of Mn/TiO$_2$-NT consisted of two peaks at 458.4 and 464.3 eV, corresponding to Ti 2p$_{3/2}$ and Ti 2p$_{1/2}$ sublevels, and the difference between these two binding energies (5.7 eV) illustrated that Ti was in the form of Ti^{4+} in the catalysts.[39] The Ti 2p binding energy of Mn/Y-doped TiO$_2$ was higher than that of Mn/TiO$_2$-NT, and shifted toward higher binding energy with an increasing amount of Y doping, suggesting that the density of the outer electron cloud of Ti decreased. Combined with the shift of the O$_\beta$ peak of the Mn/5%YTiO$_x$ catalyst, it was speculated that the chemical environments of Ti, O and Y were affected by the strong Ti–O–Y bonds in the crystal lattice, and the electron in the conduction band of TiO$_2$ could transfer to the Y element doped in TiO$_2$, leading to a reduction in the outer electron cloud density of Ti and O ions.[40]

3.6. Catalytic performances

As illustrated in Fig. 8, the Y-doped TiO$_2$ supported MnO$_x$ catalysts were examined for NO conversion and N$_2$ selectivity at 80–400 °C. It was obvious that Mn/TiO$_2$-NT exhibited the lowest SCR activity among these catalysts, and only showed 28% NO conversion at 80 °C, indicating poor low-temperature catalytic activity. While the increase in temperature can lead to a significant improvement in catalytic performance, and the NO conversion of the Mn/TiO$_2$-NT catalyst reached its maximum of 94% at 200 °C, it then decreased with further temperature increment, especially when the temperature exceeded 320 °C, which was related to the over-oxidation of NH$_3$ to nitric oxides by the O$_2$ present.[41] For the Mn/1%YTiO$_x$ catalyst, NO conversion over the entire temperature range was slightly higher than that of the Mn/TiO$_2$-NT catalyst. When the doping amount was 3%, the NO conversion was significantly improved compared with that of the Mn/1%YTiO$_x$ catalyst. It reached 62% at 80 °C, 94% at 120 °C, and showed the maximum value of 100% in the temperature range of 160–280 °C, then declined at higher temperature. However, as

Table 2 Surface component and valence states of different species from XPS data of Mn/TiO$_2$-NT and Y-doped TiO$_2$ supported MnO$_x$ catalysts

Catalyst	Mn 2p (%)			Y 3d (%)		O 1s (%)		Surface ion ratio		
	Mn^{4+}	Mn^{3+}	Mn^{2+}	Y^{3+}	Y^{2+}	O$_\alpha$	O$_\beta$	Mn^{4+}/Mn^{3+}	Y^{3+}/Y^{2+}	O$_\alpha$/O$_\beta$
Mn/TiO$_2$-NT	29.8	53.5	16.7	—	—	25.2	74.8	0.55	—	0.34
Mn/1%YTiO$_x$	45.5	37.8	16.7	66.9	33.1	30.1	69.9	1.20	2.02	0.43
Mn/3%YTiO$_x$	46.6	46.6	6.8	79.2	20.8	33.8	66.2	1.00	3.81	0.51
Mn/5%YTiO$_x$	43.2	50.7	6.1	86.7	13.3	33.9	66.1	0.85	6.52	0.51
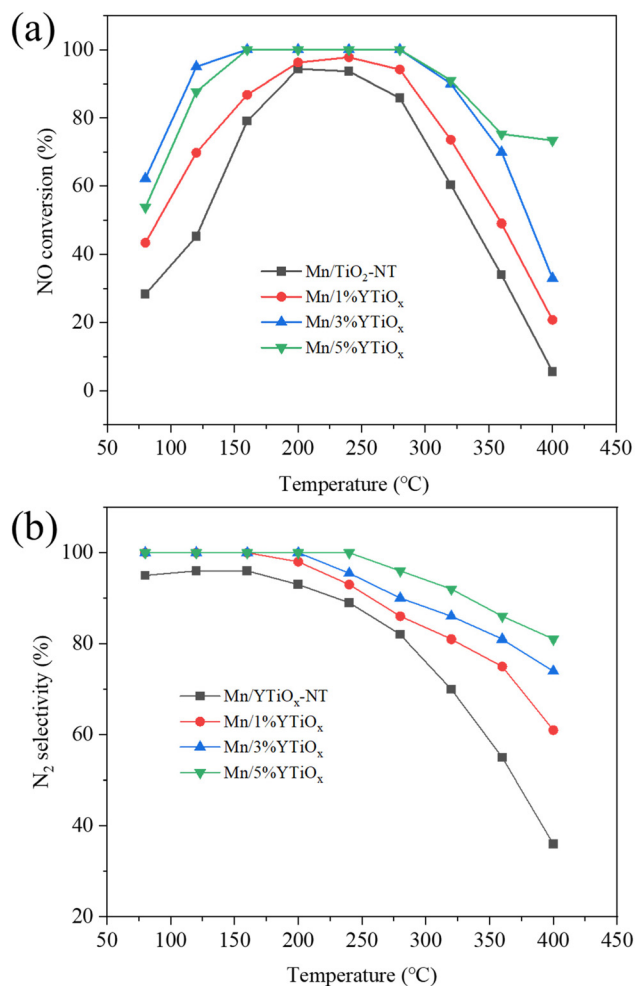
Fig. 8 NO conversion (a) and N$_2$ selectivity (b) over Y-doped TiO$_2$ supported MnO$_x$ catalysts as a function of temperature. Reaction conditions: 500 ppm NO, 500 ppm NH$_3$, 5 vol% O$_2$, and N$_2$ to balance, GHSV = 30 000 h^{-1}.

the doping amount increased to 5%, the NO conversion of the Mn/5%YTiO$_x$ catalyst in the low-temperature range (<160 °C) was lower than that of the Mn/3%YTiO$_x$ catalyst, indicating a reduction in catalytic activity. Based on the above characterization analysis, it was concluded that the improvement in low-temperature NO conversion with increased amount of Y doping from 1% to 3% could mainly be attributed to the good dispersion of MnO$_x$ and more surface Lewis acid sites and chemisorbed oxygen. While 5% Y doping showed limited promotion

on further increasing the surface chemisorbed oxygen but greatly reduced the specific surface area and Lewis acid sites of the catalyst, resulting in a decrease in catalytic ability. Besides, it was noted that the NO conversion of the Mn/5%YTiO$_x$ catalyst was higher than that of other catalysts at 320–400 °C, and still maintained NO conversion of 73% at 400 °C, which was due to more Y species also exhibiting catalytic activity in the higher temperature range. As can be seen from Table 3, the NO conversion of the Mn/3%YTiO$_x$ catalyst was higher than that of Mn-based catalysts obtained only through metal doping or construction of a 3D structure, indicating that the coupling of Y doping and 3D TiO$_2$ construction can effectively improve the catalytic ability of Mn-based catalysts.

The N$_2$ selectivity over catalysts is given in Fig. 8(b). N$_2$ selectivity remained around 90% over an Mn/TiO$_2$-NT catalyst in the temperature window of 80–160 °C, and gradually declined to only 36% at 400 °C, which could probably be attributed to the N$_2$O generated from non-selective catalytic ammonia oxidation.[47] When the doping amount was only 1%, N$_2$ selectivity was greatly increased and at least 90% of NO$_x$ was selectively converted into N$_2$ below 240 °C. Fortunately, the N$_2$ selectivity was further enhanced to some extent with doping by Y species, and Mn/5%YTiO$_x$ catalyst could maintain 100% N$_2$ selectivity in the temperature range of 80–240 °C, and more than 85% N$_2$ selectivity in the temperature range of 80–400 °C, suggesting that the bypass reaction could be restrained effectively by Y doping.

Since SO$_2$ and water vapor are considered to be the main species responsible for the deactivation of Mn-based catalysts in the SCR reaction, the tolerance to H$_2$O and SO$_2$ of Y-doped TiO$_2$ supported MnO$_x$ catalysts was investigated, and the results are exhibited in Fig. 9. As shown in Fig. 9, the resistance tests for H$_2$O and SO$_2$ were conducted at 180 °C under a GHSV of 30 000 h^{-1}, and the reaction was required to run for an hour before the addition of H$_2$O. It can be seen from the water resistance test of 11 hours with 5 vol% water vapor that NO conversion of Mn/TiO$_2$-NT declined from 80% to 50%, suggesting that there was strong competitive adsorption between water and reactants. However, the water resistance of the catalysts was enhanced with the increase in Y doping content; in particular, the NO conversion of the Mn/5%YTiO$_x$ catalyst was only reduced from 100% to 85%. NO conversion by all catalysts was restored to almost the initial value and remained at this stable level when the 5 vol% H$_2$O was turned off, indicating that the deactivation was reversible. Zhang et al.[48] found that competitive adsorption on Mn-based cata-
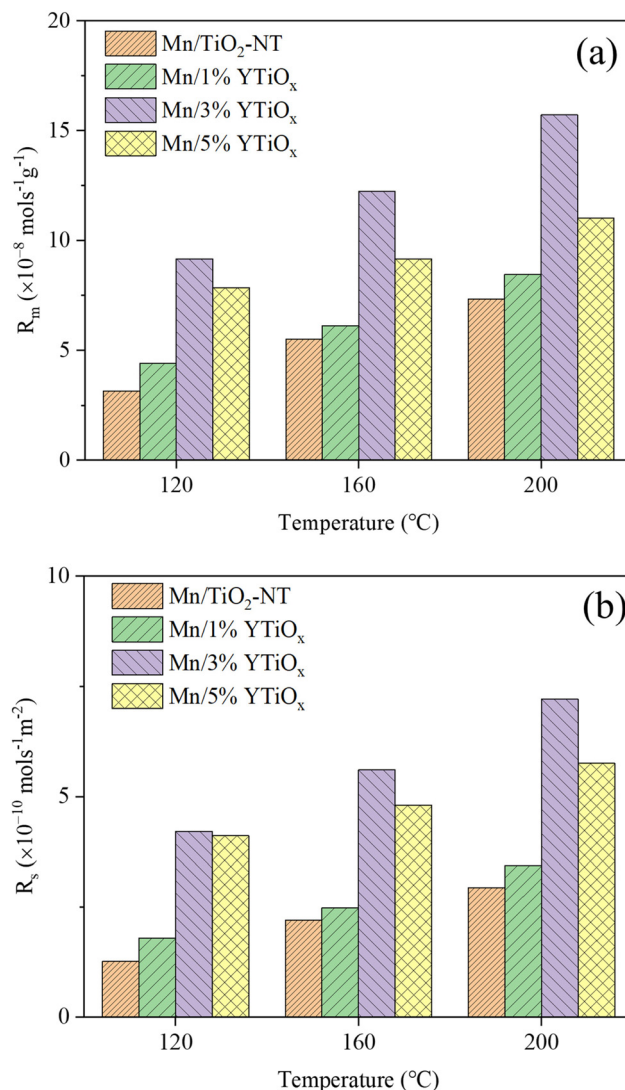
Table 3 Comparison of catalytic performance of Mn-based catalysts reported in the literature and this work

Catalyst	Reaction conditions	NO conversion (temperature range)	Ref.
Sm–Mn-0.1	0.05% NO, 0.05% NH$_3$, 5% O$_2$, 48 600 h^{-1}	90% (75–200 °C)	4
MnEu/TiO$_2$	0.06% NO, 0.06% NH$_3$, 5% O$_2$, 108 000 h^{-1}	90% (200–400 °C)	5
PrO$_x$–MnO$_x$/SAPO-34	0.08% NO, 0.08% NH$_3$, 5% O$_2$, 40 000 h^{-1}	90% (160–280 °C)	7
Tm$_{0.1}$Mn/TiO$_2$	0.05% NO, 0.05% NH$_3$, 5% O$_2$, 36 000 h^{-1}	90% (120–270 °C)	8
MnCe/TiO$_2$-FL	0.06% NO, 0.06% NH$_3$, 5% O$_2$, 100 000 h^{-1}	90% (150–250 °C)	11
Mn/TNT	0.09% NO, 0.01% NO$_2$, 0.1% NH$_3$, 10% O$_2$, 50 000 h^{-1}	90% (100–250 °C)	14
Mn$_2$Nb$_1$O$_x$	0.05% NO, 0.05% NH$_3$, 5% O$_2$, 50 000 h^{-1}	90% (125–200 °C)	42
Mn$_{0.28}$–Ce$_{0.05}$–Ti$_{0.67}$–O	0.06% NO, 0.06% NH$_3$, 3% O$_2$, 40 000 h^{-1}	92% (120–180 °C)	43
Mn$_1$–Ce$_{0.3}$/TiO$_2$–graphene	0.05% NO, 0.05% NH$_3$, 7% O$_2$, 67 000 h^{-1}	90% (140–180 °C)	44
MnFe@Ti	0.05% NO, 0.05% NH$_3$, 5% O$_2$, 30 000 h^{-1}	80% (145–260 °C)	45
MnO$_x$/TiO$_2$	0.1% NO, 0.1% NH$_3$, 3% O$_2$, 30 000 h^{-1}	90% (144–247 °C)	46
Mn/3%YTiO$_x$	0.05% NO, 0.05% NH$_3$, 5% O$_2$, 30 000 h^{-1}	90% (120–320 °C)	This work
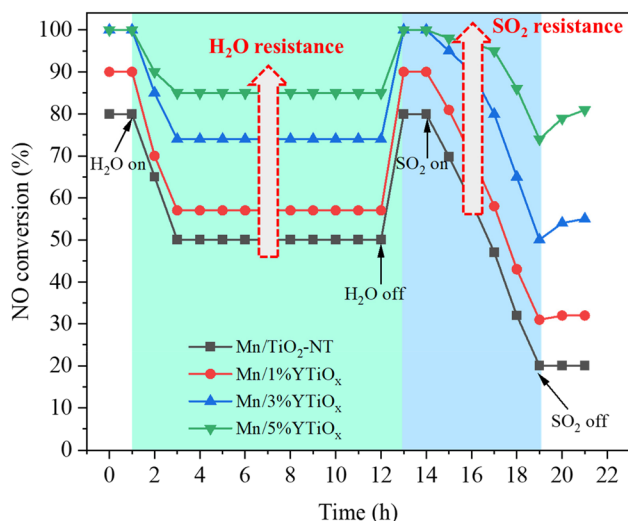
Fig. 9 Effect of SO$_2$ and H$_2$O on NO conversion of Y-doped TiO$_2$ supported MnO$_x$ catalysts. Reaction conditions: 500 ppm NO, 500 ppm NH$_3$, 5 vol% O$_2$, 100 ppm SO$_2$, 5 vol% H$_2$O, and N$_2$ to balance, GHSV = 30 000 h^{-1}.

Fig. 10 Transient rates based on the catalyst mass (a) and the specific surface area (b) of NO over catalysts at different temperatures for the NH$_3$-SCR reaction.
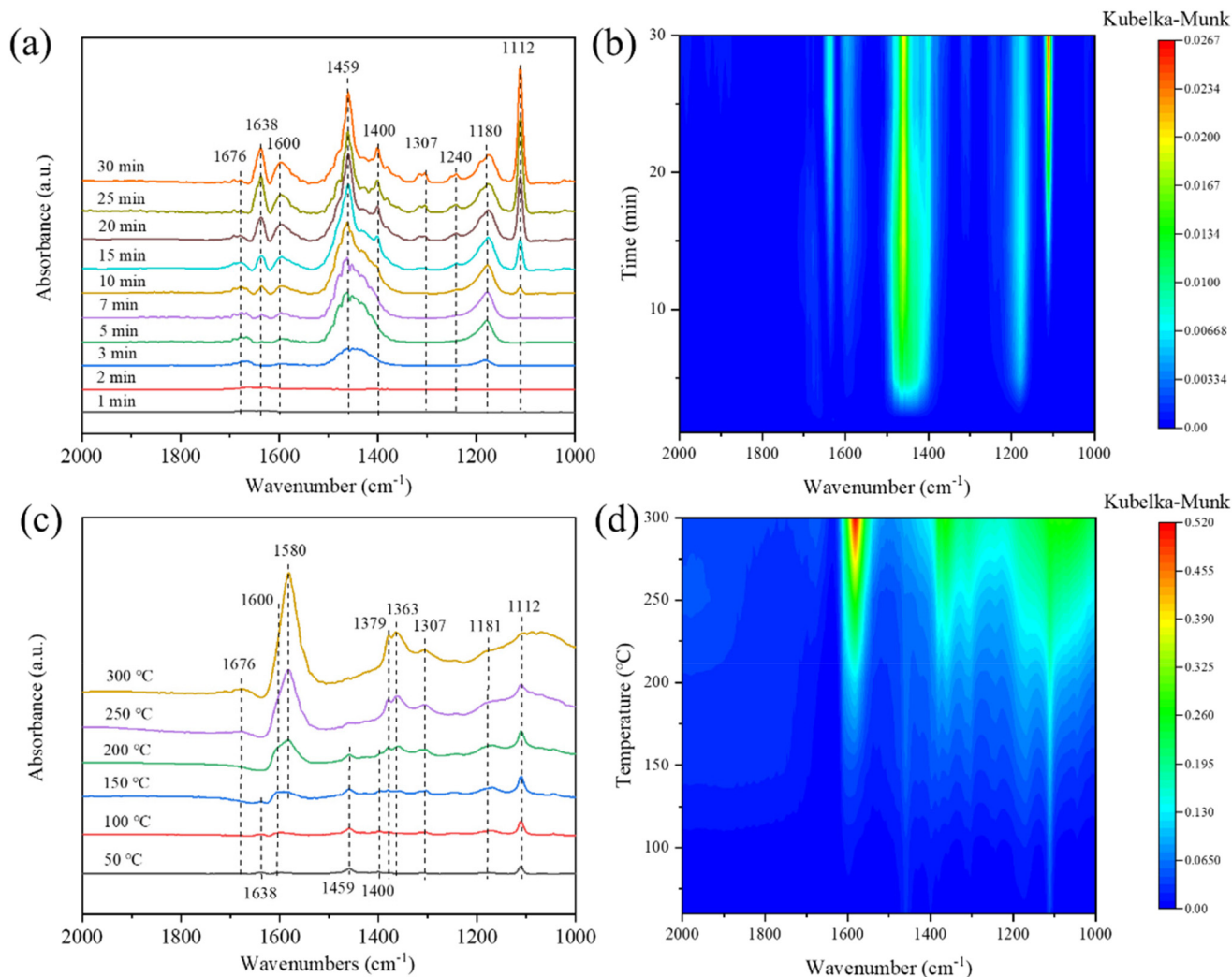
lysts main existed between NO$_x$ and H$_2$O by *in situ* DRIFT and TPD, and the labile oxygen on the catalyst surface could preferentially activate NO and restrict the adsorption of H$_2$O on the same site. Therefore, it was conjectured that the enhancement in H$_2$O resistance could be attributed to the increase in chemisorbed oxygen due to Y doping. Subsequently, SO$_2$ of 100 ppm was introduced, and NO conversion of all catalysts gradually decreased as SO$_2$ was continuously introduced. Similarly, the SO$_2$ tolerance of the catalysts improved with an increase in the Y doping amount. The NO conversion of Mn/5%YTiO$_x$ dropped from 100% to 75% after an SO$_2$ resistance test of 5 h, significantly better than that of other catalysts. But the NO conversion of Mn/5%YTiO$_x$ increased slightly after stopping the introduction of SO$_2$, suggesting the irreversible deactivation of SO$_2$ which was caused by oxidation of SO$_2$ and sulfate deposition. Combined with the results of H$_2$-TPR and XPS, it was speculated that the enhanced redox circle of Mn^{4+} + Y^{2+} ↔ Mn^{3+} + Y^{3+} could be responsible for the good SO$_2$ resistance because the electron transfer from Y^{2+} to Mn^{4+} in the

Fig. 11 *In situ* DRIFT spectra of NH$_3$ adsorption at 50 °C as a function of time (a, b) and desorption purged by N$_2$ at 50−300 °C (c, d) over the Mn/3%YTiO$_x$ catalyst.

redox circle inhibited the electron transfer from SO$_2$ to Mn^{4+}, thus hindering the oxidation of SO$_2$. In summary, the doping of Y in TiO$_2$ can significantly enhance the resistance to water and sulfur of Mn-based catalysts in the NH$_3$-SCR reaction.

3.7. *In situ* DRIFTs

3.7.1. NH$_3$ adsorption and desorption. The NH$_3$ adsorption and desorption behavior on the Mn/3%YTiO$_x$ catalyst was investigated in order to gain a deep insight into the surface acidity property over the catalyst, and the corresponding *in situ* DRIFTS spectra were collected. As depicted in Fig. 11(a and b), several peaks at 1100–1700 cm^{-1} were observed over time. The peaks at 1112, 1180 and 1600 cm^{-1} were assigned to the NH$_3$ species absorbed on Lewis acid sites.[49] The peaks at 1400, 1459 and 1638 cm^{-1} were ascribed to the NH$_4^+$ formed on Brønsted acid sites.[50] The peak at 1307 cm^{-1} was attributed to the –NH$_2$ groups generated from the de-protonation of NH$_3$ adsorbed on Lewis acid sites under the action of surface chemisorbed oxygen.[51] The peak intensity of Lewis acid and

Brønsted acid increased significantly with prolongation of time, indicating that the catalyst surface contained abundant Brønsted acid and Lewis acid sites, very consistent with the information derived from NH$_3$-TPD. The signals at 1400, 1459 and 1638 cm^{-1} related to Brønsted acid sites existed with ramping temperatures from 50 to 200 °C while they weakened to disappear above 200 °C, as shown in Fig. 11(c and d). However, the peaks at 1112, 1181 and 1600 cm^{-1} attributed to Lewis acid sites remained stable during a rise in temperature from 50 to 250 °C, and displayed a slight drop even at 300 °C, suggesting that there were still a considerable number of co-ordinated NH$_3$ species on Lewis acid sites at higher temperature. The stable presence of Lewis acid sites plays an important role in the NH$_3$-SCR reaction. Furthermore, the peak intensity at 1307 cm^{-1} ascribed to the –NH$_2$ amide groups was enhanced with ramping temperature, indicating that –NH$_2$ groups were continuously generated and remained stable in a wide temperature window. Combined with previous reports,[52] it can be considered that more surface chemisorbed oxygen

and oxygen vacancies on the Mn/3%YTiO$_x$ catalyst due to the Y doping led to fast and efficient electron mobility, promoting the activation of NH$_3$ to form –NH$_2$ species. Additionally, the formation of –NH$_2$ species may be the main reason for the improvement in N$_2$ selectivity of catalyst because the –NH$_2$ species could react with pre-adsorbed NO to generate unstable intermediates NH$_2$NO, which subsequently decomposed to N$_2$ and H$_2$O.[53] As the temperature was raised further, the peaks at 1363, 1379 and 1580 cm^{-1} appeared at 200 °C and were rapidly enhanced, which were assigned to the intermediates of NH$_3$ oxidation.[54]

3.7.2. NO + O$_2$ adsorption and desorption. *In situ* DRIFTS spectra of NH$_3$ adsorption at 50 °C as a function of time and desorption purged by N$_2$ in the temperature range from 50 °C to 300 °C over the Mn/3%YTiO$_x$ catalyst are shown in Fig. 12. With the continuous flow of NO + O$_2$, the signal at 1462 cm^{-1} was observed at the fifth minute, which was assigned to the

asymmetric stretching of trans-NO$_2$, as shown in Fig. 12(a and b).[55] Conventionally, the existence of adsorbed NO$_2$ on the catalyst was conducive to improving catalytic activity at low temperature by a "fast SCR" route.[56] As time went on, some peaks appeared and continued to increase, suggesting that the main species adsorbed on the surface were gradually changing into multiple configurations of nitrate, including bidentate nitrates (1302 cm^{-1}), free nitrate ions (1329), nitrito species (1398 cm^{-1}), monodentate nitrates (1510 cm^{-1}) and bridging nitrates (1608 cm^{-1}).[28,56–59] The formation of these nitrate species on the surface of the catalyst at low temperature meant an enhancement in NO activation capacity, which was ascribed to the abundant surface chemisorbed oxygen.[60] As depicted in Fig. 12(c and d), when the temperature was elevated, the peak attributed to the trans-NO$_2$ species (1462 cm^{-1}) decreased due to the desorption of NO$_2$, the peaks assigned to free nitrate ions (1329 cm^{-1}) decreased slightly, and the peaks attributed
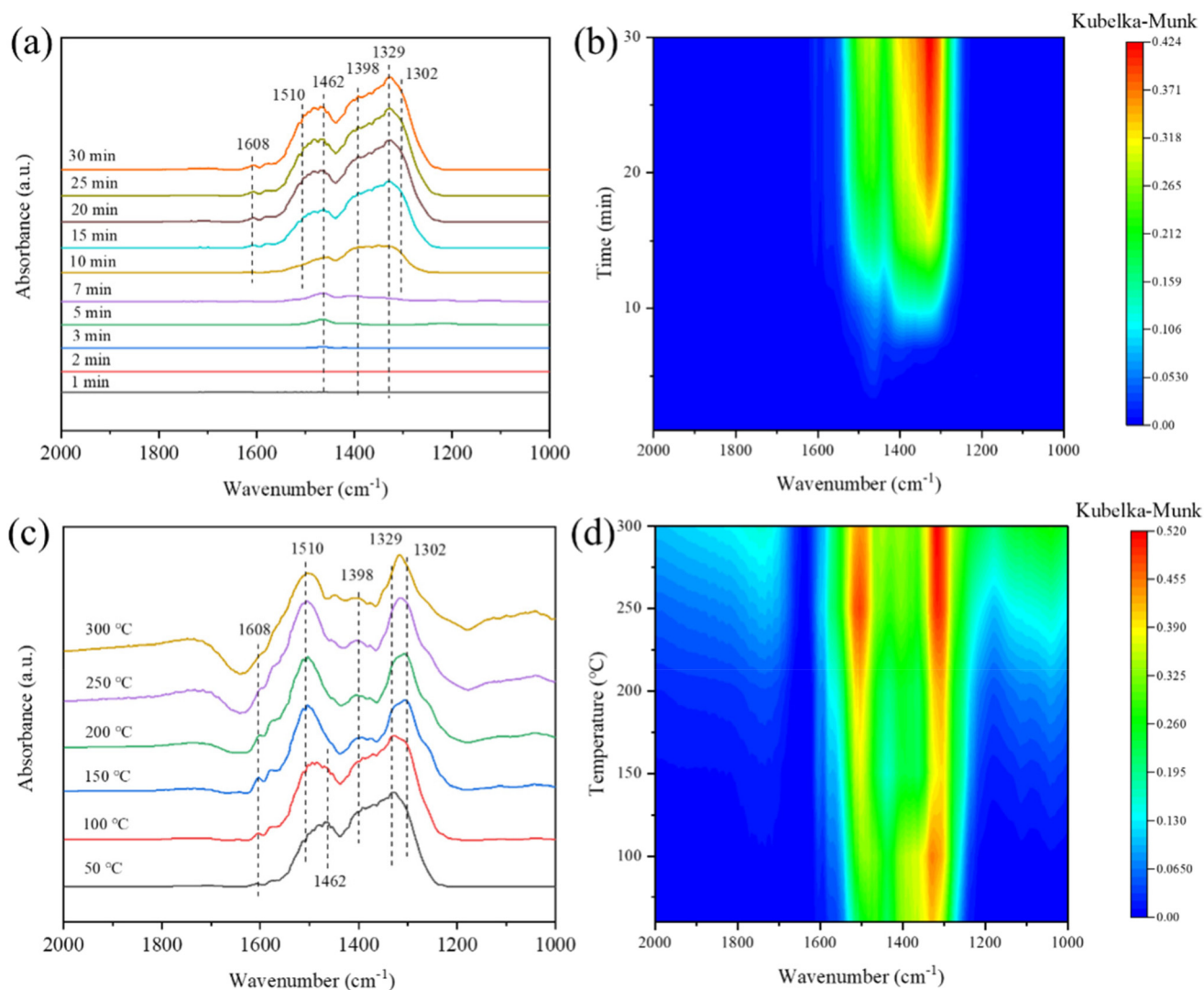

Fig. 12 *In situ* DRIFT spectra of NO + O$_2$ adsorption at 50 °C as a function of time (a, b), and desorption purged by N$_2$ at 50–300 °C (c, d) over the Mn/3%YTiO$_x$ catalyst.

to the bidentate nitrates (1302 cm^{-1}) remained unchanged from 50 to 300 °C. A marked increase in monodentate nitrates (1510 cm^{-1}) and a marked decrease in nitrito species (1398 cm^{-1}) were observed with ramping temperature, and the opposite trend in peak intensity suggested the transformation of nitrito species to monodentate nitrates, indicating that the monodentate nitrates were more stable at higher temperature. Overall, NO could be absorbed and activated by the Mn/3% YTiO$_x$ catalyst at low temperature and the generated nitrates, such as monodentate nitrates, were still stable on the surface of the catalyst at higher temperature, which may have led to excellent catalytic performance over a wide temperature range.

3.7.3. Reaction between NO + O$_2$ and NH$_3$ species. It can clearly be observed from Fig. 10, that the Mn/3%YTiO$_x$ catalyst presented the highest transient reaction rate, whether based on catalyst weight or catalyst specific area. In order to further explore the reaction mechanism over the Mn/3%YTiO$_x$ catalyst, transient reaction experiments at 180 °C over the Mn/3%YTiO$_x$

catalyst were carried out, and Fig. 13 shows the *in situ* DRIFT spectra of the transient reaction. From Fig. 13(a and b), the Mn/3%YTiO$_x$ catalyst was firstly saturated by exposure to NH$_3$ at 180 °C, and the peaks attributed to Lewis acid sites (1112, 1180 and 1600 cm^{-1}), Brønsted acid sites (1430 cm^{-1}), –NH$_2$ groups (1303 cm^{-1}) and intermediates of NH$_3$ oxidation (1366, 1379, 1584 cm^{-1}) were detected. When the NO + O$_2$ was turned on, the peaks assigned to the –NH$_2$ groups and the NH$_3$ co-ordinated on Lewis acid sites decreased gradually after 10 minutes, indicating the involvement and consumption of the two species in the NH$_3$-SCR reaction. While consumption had not happened for the adsorbed NH$_4^+$ groups coordinated on Brønsted acid sites, illustrating that Brønsted acid sites did not play a vital role in the reaction. Additionally, this conclusion can also be verified from the results of NH$_3$-TPD and activity tests, in which the reduction of the amount of Brønsted acid sites due to Y doping had no obvious effect on the NO conversion of the catalysts. Besides, the appearance
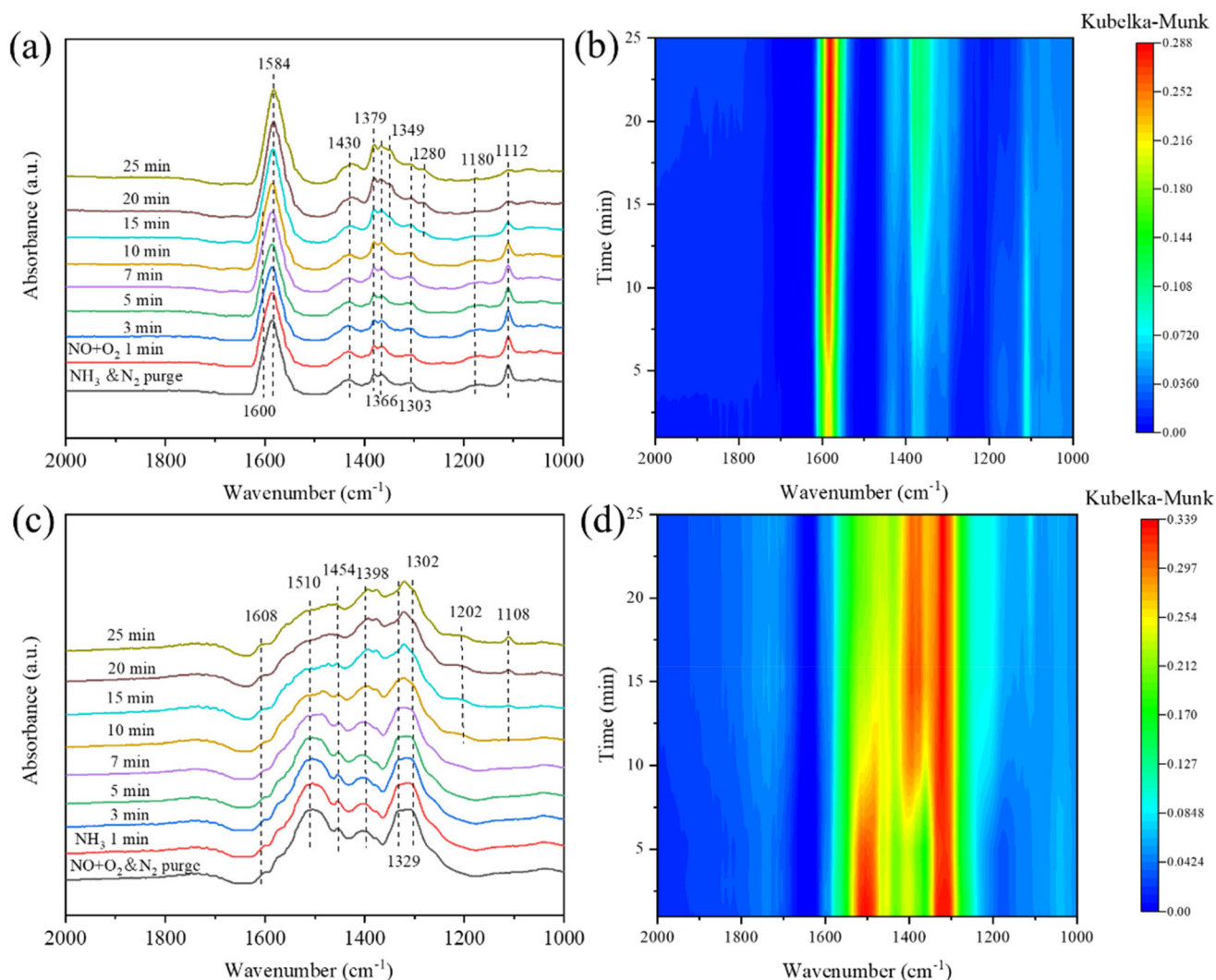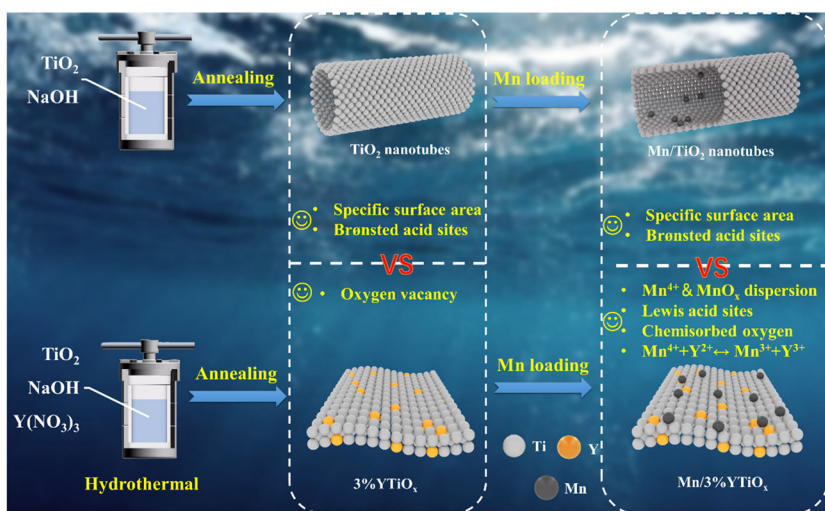

Fig. 13 *In situ* DRIFT spectra of transient reaction at 180 °C over the Mn/3%YTiO$_x$ catalyst between NO + O$_2$ and pre-adsorbed NH$_3$ (a, b) and NH$_3$ and pre-adsorbed NO + O$_2$ (c, d) as a function of time.

Scheme 1 Schematic diagram of the synthesis process for the Mn/3%TiO$_x$ catalyst.

and enhancement of peaks at 1280 and 1349 cm^{-1} were attributed to the formation and accumulation of linear nitrite and ionic nitrate species, respectively.[61,62] The above changes elucidated that the adsorbed NH$_3$ species coordinated on Lewis acid sites and –NH$_2$ groups were the main active species, and adsorbed NH$_3$ species can easily react with nitrite species adsorbed on the surface at 180 °C according to the Langmuir–Hinshelwood (L–H) mechanism. While the formation of –NH$_2$ groups represented the moderate oxidation of NH$_3$ in the NH$_3$-SCR reaction, and it can directly react with the gaseous NO to form H$_2$O and N$_2$ following an Eley–Rideal (E–R) reaction pathway, which was favorable for good N$_2$ selectivity.[63] Considering that the formation of –NH$_2$ groups arose mainly from the oxidation of surface chemisorbed oxygen, it was speculated that the increase in N$_2$ selectivity with Y doping was mainly related to the increase in Lewis acid sites and surface chemisorbed oxygen.

The transient reaction at 180 °C between pre-adsorbed NO + O$_2$ and NH$_3$ was detected by *in situ* DRIFTS spectra, and the results are depicted in Fig. 13(c and d). Free nitrate ions (1329), nitrito species (1398 cm^{-1}), bidentate nitrates (1302 cm^{-1}), monodentate nitrates (1510 cm^{-1}), trans-NO$_2$ (1454 cm^{-1}) and bridging nitrates (1608 cm^{-1}) were formed after the pre-adsorption of NO + O$_2$. After the ammonia was pumped in, the peak intensities of bidentate nitrate, nitrito species and bridging nitrates seldom varied, suggesting they seldom participated in the reaction. While, monodentate nitrate and free nitrate ions showed a significant decrease in intensity from 7 min to 25 min, manifesting that monodentate nitrate and free nitrate ions may be the main reactive intermediate species in the NH$_3$-SCR reaction. Moreover, the peak intensities of 1108 and 1202 cm^{-1} appeared and increased gradually from 7 min to 25 min, which were assigned to the coordinated NH$_3$ due to the introduction of NH$_3$.

3.7.4. Possible reaction mechanism. As shown in Scheme 1, 3%YTiO$_x$ nanosheets were obtained by doping 3% Y

in the process of the traditional hydrothermal synthesis of titanium nanotubes, which were different in composition from the nanotubes and had more oxygen vacancies. Moreover, the Mn/3%YTiO$_x$ catalyst had a better redox property and more Lewis acid sites than the Mn/TiO$_2$-NT catalyst, which resulted in improvements in NO conversion, N$_2$ selectivity and H$_2$O/SO$_2$ resistance. A possible NH$_3$-SCR reaction mechanism over the Mn/3%YTiO$_x$ catalyst was proposed by means of *in situ* DRIFTS. As depicted in Scheme 2, E–R and L–H reaction mechanisms co-existed in the NH$_3$-SCR reaction process over the catalyst. In case of the E–R reaction mechanism, abundant coordinated NH$_3$ adsorbed on Lewis acid sites was activated by surface chemisorbed oxygen and converted to –NH$_2$ groups,
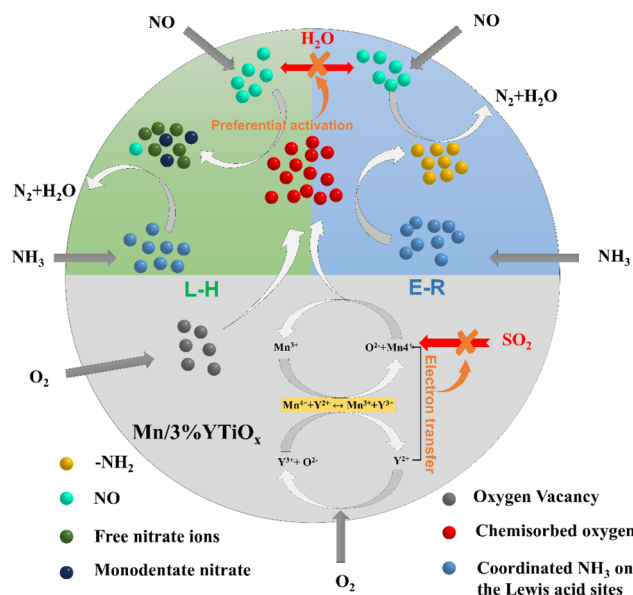
Scheme 2 Schematic illustration of possible NH$_3$-SCR reaction mechanism over the Mn/3%YTiO$_x$ catalyst at 180 °C.

which can directly react with gaseous NO to form N_2 and H_2O. For the L–H reaction mechanism, gaseous NO was adsorbed and oxidized to monodentate nitrate and free nitrate ions, which reacted with adsorbed NH_3 to form N_2 and H_2O. From the changes in species in the transient reaction (Fig. 13), the L–H reaction mechanism predominated. Electron transfer from Y^{2+} to Mn^{4+} inhibited electron transfer from SO_2 to Mn, thus effectively avoiding poisoning from SO_2. The preferential adsorption and activation of NO were promoted by the surface chemisorbed oxygen, which effectively inhibited the competitive adsorption between NO and H_2O.

4. Conclusions

Y-Doped TiO_x with a 3D structure was prepared by adding Y to a mixture of TiO_2 powder and NaOH during the alkaline hydrothermal synthesis of titanium nanotubes, followed by supporting MnO_x for the low-temperature NH_3-SCR reaction. The effect of Y doping on the physicochemical properties of synthesized 3D TiO_x and the further effect on catalytic performance of Mn/Y-doped TiO_x catalysts were investigated through a series of analytical techniques and performance tests, including NO conversion, N_2 selectivity and H_2O/SO_2 resistance. The results showed that the synthesized 3D TiO_x gradually transformed from nanotubes to nanosheets with an increase in Y doping, leading to a reduction in specific surface area and Brønsted acid sites, but NO conversion by Mn/Y-doped TiO_x catalysts exhibited a volcano-type tendency with an increase in the Y content. An appropriate amount of Y doping, such as 3%, can significantly improve the dispersion of MnO_x, and increase the concentration of Mn^{4+}, Lewis acid sites and surface chemisorbed oxygen of catalysts, thus effectively enhancing the catalytic ability for NH_3-SCR. The Mn/3%$YTiO_x$ catalyst showed NO conversion and N_2 selectivity above 90% in a wide temperature window from 120 to 320 °C under a GHSV of 30 000 h^{-1}. However, an excessive amount of Y doping, such as 5%, could result in a noticeable decrease in specific surface area, Lewis acid sites and surface Mn^{4+} content of the catalyst, which was detrimental to the NH_3-SCR. Besides, the N_2 selectivity and H_2O/SO_2 tolerance of catalysts were distinctly enhanced with an increase in Y doping, which were mainly ascribed to the abundant surface chemisorbed oxygen and the electron transfer from Y to Mn. An *in situ* DRIFTS study demonstrated that Lewis acid sites, –NH_2 species, monodentate nitrate and free nitrate ions were the main reactive intermediate species of the NH_3-SCR reaction over the Mn/3% $YTiO_x$ catalyst, and the reaction followed the Langmuir–Hinshelwood (L–H) and Eley–Rideal (E–R) reaction mechanisms, between which the L–H reaction mechanism predominated.

Conflicts of interest

The authors declare that they have no known competing financial interests or personal relationships that could have appeared to influence the work reported in this paper.

References

1 X. Huang, F. Dong, G. Zhang, Y. Guo and Z. Tang, A strategy for constructing highly efficient yolk-shell Ce@Mn@TiO_x catalyst with dual active sites for low-temperature selective catalytic reduction of NO with NH_3, *Chem. Eng. J.*, 2021, **419**, 129572.

2 G. Zhang, W. Han, F. Dong, L. Zong, G. Lu and Z. Tang, One pot synthesis of a highly efficient mesoporous ceria–titanium catalyst for selective catalytic reduction of NO, *RSC Adv.*, 2016, **6**, 76556–76567.

3 R. Jin, Y. Liu, Y. Wang, W. Cen, Z. Wu, H. Wang and X. Weng, The role of cerium in the improved SO_2 tolerance for NO reduction with NH_3 over Mn-Ce/TiO_2 catalyst at low temperature, *Appl. Catal., B*, 2014, **148–149**, 582–588.

4 D. Meng, W. Zhan, Y. Guo, Y. Guo, L. Wang and G. Lu, A highly effective catalyst of Sm-MnO_x for the NH_3-SCR of NO_x at low temperature: Promotional role of Sm and its catalytic performance, *ACS Catal.*, 2015, **5**, 5973–5983.

5 J. Liu, R. T. Guo, M. Y. Li, P. Sun, S. M. Liu, W. G. Pan, S. W. Liu and X. Sun, Enhancement of the SO_2 resistance of Mn/TiO_2 SCR catalyst by Eu modification: A mechanism study, *Fuels*, 2018, **223**, 385–393.

6 P. Sun, R. T. Guo, S. M. Liu, S. X. Wang, W. G. Pan and M. Y. Li, The enhanced performance of MnO_x catalyst for NH_3-SCR reaction by the modification with Eu, *Appl. Catal., A*, 2017, **531**, 129–138.

7 C. Yu, B. Huang, L. Dong, F. Chen, Y. Yang, Y. Fan, Y. Yang, X. Liu and X. Wang, Effect of Pr/Ce addition on the catalytic performance and SO_2 resistance of highly dispersed MnO_x/SAPO-34 catalyst for NH_3-SCR at low temperature, *Chem. Eng. J.*, 2017, **316**, 1059–1068.

8 C. H. Niu, B. R. Wang, Y. Xing, W. Su, C. He, L. Xiao, Y. R. Xu, S. Q. Zhao, Y. H. Cheng and J. W. Shi, Thulium modified MnO_x/TiO_2 catalyst for the low-temperature selective catalytic reduction of NO with ammonia, *J. Cleaner Prod.*, 2021, **290**, 125858.

9 S. Zhang, X. Liu, Q. Zhong and Y. Yao, Effect of Y doping on oxygen vacancies of TiO_2 supported MnO_x for selective catalytic reduction of NO with NH_3 at low temperature, *Catal. Commun.*, 2012, **25**, 7–11.

10 L. Zong, G. Zhang, J. Zhao, F. Dong, J. Zhang and Z. Tang, Morphology-controlled synthesis of 3D flower-like TiO_2 and the superior performance for selective catalytic reduction of NO_x with NH_3, *Chem. Eng. J.*, 2018, **343**, 500–511.

11 B. Qin, R. T. Guo, J. Zhou, L. G. Wei, T. Y. Yin and W. G. Pan, A novel flower-like MnCe/TiO$_2$ catalyst with controlled morphology for low-temperature selective catalytic reduction of NO with NH$_3$, *Appl. Surf. Sci.*, 2022, **598**, 153823.

12 K. Cheng, W. Song, Y. Cheng, J. Liu, Z. Zhao and Y. Wei, Selective catalytic reduction over size-tunable rutile TiO$_2$ nanorod microsphere-supported CeO$_2$ catalysts, *Catal. Sci. Technol.*, 2016, **6**, 4478–4490.

13 Q. Li, X. Li, W. Li, L. Zhong, C. Zhang, Q. Fang and G. Chen, Effect of preferential exposure of anatase TiO$_2$ {001} facets on the performance of Mn-Ce/TiO$_2$ catalysts for low-temperature selective catalytic reduction of NO$_x$ with NH$_3$, *Chem. Eng. J.*, 2019, **369**, 26–34.

14 T. Boningari, D. K. Pappas and P. G. Smirniotis, Metal oxide-confined interweaved titania nanotubes M/TNT (M = Mn, Cu, Ce, Fe, V, Cr, and Co) for the selective catalytic reduction of NO$_x$ in the presence of excess oxygen, *J. Catal.*, 2018, **365**, 320–333.

15 X. Chen, P. Wang, P. Fang, H. Wang, C. Cen, W. Zeng and Z. Wu, Design strategies for SCR catalysts with improved N$_2$ selectivity: the significance of nano-confining effects by titanate nanotubes, *Environ. Sci.: Nano*, 2017, **4**, 437–447.

16 P. Wang, H. Wang, X. Chen and Z. Wu, Design strategies for a denitrification catalyst with improved resistance against alkali poisoning: The significance of nanoconfining spaces and acid-base balance, *ChemCatChem*, 2016, **8**, 787–797.

17 X. B. Chen, P. L. Wang, P. Fang, T. Y. Ren, Y. Liu, C. P. Cen, H. Q. Wang and Z. B. Wu, Tuning the property of Mn-Ce composite oxides by titanate nanotubes to improve the activity, selectivity and SO$_2$/H$_2$O tolerance in middle temperature NH$_3$-SCR reaction, *Fuel Process. Technol.*, 2017, **167**, 221–228.

18 R. Yuan, B. Zhou, D. Hua and C. Shi, Enhanced photocatalytic degradation of humic acids using Al and Fe co-doped TiO$_2$ nanotubes under UV/ozonation for drinking water purification, *J. Hazard. Mater.*, 2013, **262**, 527–538.

19 F. Jiang, S. Zheng, L. An and H. Chen, Effect of calcination temperature on the adsorption and photocatalytic activity of hydrothermally synthesized TiO$_2$ nanotubes, *Appl. Surf. Sci.*, 2012, **258**, 7188–7194.

20 B. Erjavec, R. Kaplan, P. Djinović and A. Pintar, Catalytic wet air oxidation of bisphenol A model solution in a trickle-bed reactor over titanate nanotube-based catalysts, *Appl. Catal., B*, 2013, **132**, 342–352.

21 X. M. Liu, S. Y. Fu and C. J. Huang, Synthesis, characterization and magnetic properties of β-MnO$_2$ nanorods, *Powder Technol.*, 2005, **154**, 120–124.

22 S. Mathew, P. Ganguly, V. Kumaravel, J. Harrison, S. J. Hinder, J. Bartlett and S. C. Pillai, Effect of chalcogens (S, Se, and Te) on the anatase phase stability and photocatalytic antimicrobial activity of TiO$_2$, *Mater. Today: Proc.*, 2020, **33**, 2458–2464.

23 W. Hu, L. Li, G. Li, Y. Liu and R. L. Withers, Atomic-scale control of TiO$_6$ octahedra through solution chemistry towards giant dielectric response, *Sci. Rep.*, 2014, **4**, 1–9.

24 Y. Zhong, S. Chang and G. Dong, Preparation and characterization of a novel double-walled Na$_2$(TiO)SiO$_4$ nanotube by hydrothermal process with CTAB as an assistant, *Microporous Mesoporous Mater.*, 2017, **239**, 70–77.

25 G. Srinivas, Y. Zhu, R. Piner, N. Skipper, M. Ellerby and R. Ruoff, Synthesis of graphene-like nanosheets and their hydrogen adsorption capacity, *Carbon*, 2010, **48**, 630–635.

26 X. Chen, H. Wang, Z. Wu, Y. Liu and X. Weng, Novel H$_2$Ti$_{12}$O$_{25}$-confined CeO$_2$ catalyst with remarkable resistance to alkali poisoning based on the "shell protection effect", *J. Phys. Chem. C*, 2011, **115**, 17479–17484.

27 L. Q. Weng, S. H. Song, S. Hodgson, A. Baker and J. Yu, Synthesis and characterisation of nanotubular titanates and titania, *J. Eur. Ceram. Soc.*, 2006, **26**, 1405–1409.

28 G. Cheng, X. Liu, X. Song, X. Chen, W. Dai, R. Yuan and X. Fu, Visible-light-driven deep oxidation of NO over Fe doped TiO$_2$ catalyst: Synergic effect of Fe and oxygen vacancies, *Appl. Catal., B*, 2020, **277**, 119196.

29 G. B. Sun, K. Hidajat, X. S. Wu and S. Kawi, A crucial role of surface oxygen mobility on nanocrystalline Y$_2$O$_3$ support for oxidative steam reforming of ethanol to hydrogen over Ni/Y$_2$O$_3$ catalysts, *Appl. Catal., B*, 2008, **81**, 303–312.

30 F. Dong, W. Han, Y. Guo, W. Han and Z. Tang, CeCoO$_x$-MNS catalyst derived from three-dimensional mesh nanosheet Co-based metal-organic frameworks for highly efficient catalytic combustion of VOCs, *Chem. Eng. J.*, 2021, **405**, 126948.

31 E. Wada, M. Kitano, K. Nakajima and M. Hara, Effect of preparation conditions on the structural and acid catalytic properties of protonated titanate nanotubes, *J. Mater. Chem. A*, 2013, **1**, 12768–12774.

32 M. Kitano, E. Wada, K. Nakajima, S. Hayashi, S. Miyazaki, H. Kobayashi and M. Hara, Protonated titanate nanotubes with Lewis and Brønsted acidity: Relationship between nanotube structure and catalytic activity, *Chem. Mater.*, 2013, **25**, 385–393.

33 Y. J. Kim, H. J. Kwon, I. Heo, I.-S. Nam, B. K. Cho, J. W. Choung, M.-S. Cha and G. K. Yeo, Mn-Fe/ZSM5 as a low-temperature SCR catalyst to remove NO$_x$ from diesel engine exhaust, *Appl. Catal., B*, 2012, **126**, 9–21.

34 F. Liu, H. He, Y. Ding and C. Zhang, Effect of manganese substitution on the structure and activity of iron titanate catalyst for the selective catalytic reduction of NO with NH$_3$, *Appl. Catal., B*, 2009, **93**, 194–204.

35 Q. Chen, F. El Gabaly, F. Aksoy Akgul, Z. Liu, B. S. Mun, S. Yamaguchi and A. Braun, Observation of oxygen vacancy filling under water vapor in ceramic proton conductors in situ with ambient pressure XPS, *Chem. Mater.*, 2013, **25**, 4690–4696.

36 S. Ali, L. Chen, Z. Li, T. Zhang, R. Li, S. u. H. Bakhtiar, X. Leng, F. Yuan, X. Niu and Y. Zhu, Cu$_x$-Nb$_{1.1-x}$ (x = 0.45, 0.35, 0.25, 0.15) bimetal oxides catalysts for the low temperature selective catalytic reduction of NO with NH$_3$, *Appl. Catal., B*, 2018, **236**, 25–35.

37 Z. P. Zhang, R. M. Li, M. J. Wang, Y. S. Li, Y. M. Tong, P. P. Yang and Y. J. Zhu, Two steps synthesis of CeTiO$_x$

oxides nanotube catalyst: Enhanced activity, resistance of SO_2 and H_2O for low temperature NH_3-SCR of NO_x, *Appl. Catal., B*, 2021, **282**, 119542.

38 X. Ma, X. Wang, L. Xu and F. Chen, Oxygen vacancy clusters enriched TiO_2 with low Pt content for superior photocatalytic activity, *Catal. Lett.*, 2022, **152**, 2585–2589.

39 T. Kubo and A. Nakahira, Local structure of TiO_2-derived nanotubes prepared by the hydrothermal process, *J. Phys. Chem. C*, 2008, **112**, 1658–1662.

40 X. Li, X. Zou, Z. Qu, Q. Zhao and L. Wang, Photocatalytic degradation of gaseous toluene over Ag-doping TiO_2 nanotube powder prepared by anodization coupled with impregnation method, *Chemosphere*, 2011, **83**, 674–679.

41 K. Gora-Marek, K. Brylewska, K. A. Tarach, M. Rutkowska, M. Jablonska, M. Choi and L. Chmielarz, IR studies of Fe modified ZSM-5 zeolites of diverse mesopore topologies in the terms of their catalytic performance in NH_3-SCR and NH_3-SCO processes, *Appl. Catal., B*, 2015, **179**, 589–598.

42 Z. Lian, F. Liu, H. He, X. Shi, J. Mo and Z. Wu, Manganese-niobium mixed oxide catalyst for the selective catalytic reduction of NO_x with NH_3 at low temperatures, *Chem. Eng. J.*, 2014, **250**, 390–398.

43 Z. Y. Sheng, Y. F. Hu, J. M. Xue, X. M. Wang and W. P. Liao, SO_2 poisoning and regeneration of Mn-Ce/TiO_2 catalyst for low temperature NO_x reduction with NH_3, *J. Rare Earths*, 2012, **30**, 676–682.

44 X. Lu, C. Song, S. Jia, Z. Tong, X. Tang and Y. Teng, Low-temperature selective catalytic reduction of NO_x with NH_3 over cerium and manganese oxides supported on TiO_2-graphene, *Chem. Eng. J.*, 2015, **260**, 776–784.

45 Z. Cai, G. Zhang, Z. Tang and J. Zhang, $MnFeO_x$@TiO_2 Nanocages for selective catalytic reduction of NO with NH_3 at low temperature, *ACS Appl. Nano Mater.*, 2021, **4**, 6201–6211.

46 B. Jiang, Y. Liu and Z. Wu, Low-temperature selective catalytic reduction of NO on MnO_x/TiO_2 prepared by different methods, *J. Hazard. Mater.*, 2009, **162**, 1249–1254.

47 Y. Xin, H. Li, N. Zhang, Q. Li, Z. Zhang, X. Cao, P. Hu, L. Zheng and J. A. Anderson, Molecular-level insight into selective catalytic reduction of NO_x with NH_3 to N_2 over a highly efficient bifunctional V-alpha-MnO_x catalyst at low temperature, *ACS Catal.*, 2018, **8**, 4937–4949.

48 N. Q. Zhang, L. C. Li, Y. Z. Guo, J. D. He, R. Wu, L. Y. Song, G. Z. Zhang, J. S. Zhao, D. S. Wang and H. He, A MnO_2-based catalyst with H_2O resistance for NH_3-SCR: Study of catalytic activity and reactants-H_2O competitive adsorption, *Appl. Catal., B*, 2020, **270**, 118860.

49 Z. Fan, J. W. Shi, C. Gao, G. Gao, B. Wang, Y. Wang, C. He and C. Niu, Gd-modified MnO_x for the selective catalytic reduction of NO by NH_3: The promoting effect of Gd on the catalytic performance and sulfur resistance, *Chem. Eng. J.*, 2018, **348**, 820–830.

50 C. Liu, L. Chen, J. Li, L. Ma, H. Arandiyan, Y. Du, J. Xu and J. Hao, Enhancement of activity and sulfur resistance of CeO_2 supported on TiO_2-SiO_2 for the selective catalytic reduction of NO by NH_3, *Environ. Sci. Technol.*, 2012, **46**, 6182–6189.

51 N. Y. Topsøe, Mechanism of the selective catalytic reduction of nitric oxide by ammonia elucidated by in situ on-line Fourier transform infrared spectroscopy, *Science*, 1994, **265**, 1217–1219.

52 F. Liu and H. He, Structure-activity relationship of iron titanate catalysts in the selective catalytic reduction of NO_x with NH_3, *J. Phys. Chem. C*, 2010, **114**, 16929–16936.

53 F. Yan, Y. Wang, J. Zhang, Z. Lin, J. Zheng and F. Huang, Schottky or Ohmic metal-semiconductor contact: Influence on photocatalytic efficiency of Ag/ZnO and Pt/ZnO model systems, *ChemSusChem*, 2014, **7**, 101–104.

54 L. Ma, C. Y. Seo, M. Nahata, X. Chen, J. Li and J. W. Schwank, Shape dependence and sulfate promotion of CeO_2 for selective catalytic reduction of NO_x with NH_3, *Appl. Catal., B*, 2018, **232**, 246–259.

55 M. Casapu, O. Kröcher, M. Mehring, M. Nachtegaal, C. Borca, M. Harfouche and D. Grolimund, Characterization of Nb-containing MnO_x-CeO_2 catalyst for low-temperature selective catalytic reduction of NO with NH_3, *J. Phys. Chem. C*, 2010, **114**, 9791–9801.

56 J. Liu, X. Y. Li, Q. D. Zhao, J. Ke, H. N. Xiao, X. J. Lv, S. M. Liu, M. Tade and S. B. Wang, Mechanistic investigation of the enhanced NH_3-SCR on cobalt-decorated Ce-Ti mixed oxide: In situ FTIR analysis for structure-activity correlation, *Appl. Catal., B*, 2017, **200**, 297–308.

57 L. Sheng, Z. Ma, S. Chen, J. Lou, C. Li, S. Li, Z. Zhang, Y. Wang and H. Yang, Mechanistic insight into N_2O formation during NO reduction by NH_3 over Pd/CeO_2 catalyst in the absence of O_2, *Chin. J. Catal.*, 2019, **40**, 1070–1077.

58 X. Weng, X. Dai, Q. Zeng, Y. Liu and Z. Wu, DRIFT studies on promotion mechanism of $H_3PW_{12}O_{40}$ in selective catalytic reduction of NO with NH_3, *J. Colloid Interface Sci.*, 2016, **461**, 9–14.

59 Z. R. Ma, X. D. Wu, Z. C. Si, D. Weng, J. Ma and T. F. Xu, Impacts of niobia loading on active sites and surface acidity in NbO_x/CeO_2-ZrO_2 NH_3-SCR catalysts, *Appl. Catal., B*, 2015, **179**, 380–394.

60 X. M. Wu, X. L. Yu, Z. W. Huang, H. Z. Shen and G. H. Jing, MnO_x-decorated VO_x/CeO_2 catalysts with preferentially exposed {110} facets for selective catalytic reduction of NO_x by NH_3, *Appl. Catal., B*, 2020, **268**, 118419.

61 L. Liu, B. Liu, L. Dong, J. Zhu, H. Wan, K. Sun, B. Zhao, H. Zhu, L. Dong and Y. Chen, In situ FT-infrared investigation of CO or/and NO interaction with CuO/$Ce_{0.67}Zr_{0.33}O_2$ catalysts, *Appl. Catal., B*, 2009, **90**, 578–586.

62 W. Yang, R. Zhang, B. Chen, D. Duprez and S. Royer, New aspects on the mechanism of C_3H_6 selective catalytic reduction of NO in the presence of O_2 over $LaFe_{1-x}$(Cu, Pd)$_xO_{3-\delta}$ perovskites, *Environ. Sci. Technol.*, 2012, **46**, 11280–11288.

63 Z. Ma, D. Weng, X. Wu and Z. Si, Effects of WO_x modification on the activity, adsorption and redox properties of CeO_2 catalyst for NO_x reduction with ammonia, *J. Environ. Sci.*, 2012, **24**, 1305–1316.